AGU PUBLICATIONS

JGR

Journal of Geophysical Research: Atmospheres

RESEARCH ARTICLE
10.1002/2014JD022591

Key Points:
- NOAA/ESRL aircraft measurements over North America are summarized
- Seasonal cycle of CO_2 between <4000 masl is strongly impacted by surface fluxes
- Meridional and seasonal changes in transport modulate CO_2 seasonal cycle

Correspondence to:
C. Sweeney,
colm.sweeney@noaa.gov

Citation:
Sweeney, C., et al. (2015), Seasonal climatology of CO_2 across North America from aircraft measurements in the NOAA/ESRL Global Greenhouse Gas Reference Network, *J. Geophys. Res. Atmos.*, *120*, doi:10.1002/2014JD022591.

Received 18 SEP 2014
Accepted 5 APR 2015
Accepted article online 9 APR 2015

Seasonal climatology of CO_2 across North America from aircraft measurements in the NOAA/ESRL Global Greenhouse Gas Reference Network

Colm Sweeney[1,2], Anna Karion[1,2], Sonja Wolter[1,2], Timothy Newberger[1,2], Doug Guenther[1,2], Jack A. Higgs[2], Arlyn Elyzabeth Andrews[2], Patricia M. Lang[2], Don Neff[1,2], Edward Dlugokencky[2], John B. Miller[1,2], Stephen A. Montzka[2], Ben R. Miller[1], Ken Alan Masarie[2], Sebastien Christophe Biraud[3], Paul C. Novelli[2], Molly Crotwell[1], Andrew M. Crotwell[1,2], Kirk Thoning[2], and Pieter P. Tans[2]

[1]University of Colorado, Cooperative Institute for Research in Environmental Sciences, Boulder, Colorado, USA, [2]National Oceanic and Atmospheric Administration, Earth System Research Laboratory, Boulder, Colorado, USA, [3]Lawrence Berkeley National Laboratory, Berkeley, California, USA

Abstract Seasonal spatial and temporal gradients for the CO_2 mole fraction over North America are examined by creating a climatology from data collected 2004–2013 by the NOAA/ESRL Global Greenhouse Gas Reference Network Aircraft Program relative to trends observed for CO_2 at the Mauna Loa Observatory. The data analyzed are from measurements of air samples collected in specially fabricated flask packages at frequencies of days to months at 22 sites over continental North America and shipped back to Boulder, Colorado, for analysis. These measurements are calibrated relative to the CO_2 World Meteorological Organization mole fraction scale. The climatologies of CO_2 are compared to climatologies of CO, CH_4, SF_6, N_2O (which are also measured from this sampling program), and winds to understand the dominant transport and chemical and biological processes driving changes in the spatial and temporal mole fractions of CO_2 as air passes over continental North America. The measurements show that air masses coming off the Pacific on the west coast of North America are relatively homogeneous with altitude. As air masses flow eastward, the lower section from the surface to 4000 m above sea level (masl) becomes distinctly different from the 4000–8000 masl section of the column. This is due in part to the extent of the planetary boundary layer, which is directly impacted by continental sources and sinks, and to the vertical gradient in west-to-east wind speeds. The slowdown and southerly shift in winds at most sites during summer months amplify the summertime drawdown relative to what might be expected from local fluxes. This influence counteracts the dilution of summer time CO_2 drawdown (known as the "rectifier effect") as well as changes the surface influence "footprint" for each site. An early start to the summertime drawdown, a pronounced seasonal cycle in the column mean (500 to 8000 masl), and small vertical gradients in CO_2, CO, CH_4, SF_6, and N_2O at high-latitude western sites such as Poker Flat, Alaska, suggest recent influence of transport from southern latitudes and not local processes. This transport pathway provides a significant contribution to the large seasonal cycle observed in the high latitudes at all altitudes sampled. A sampling analysis of the NOAA/ESRL CarbonTracker model suggests that the average sampling resolution of 22 days is sufficient to get a robust estimate of mean seasonal cycle of CO_2 during this 10 year period but insufficient to detect interannual variability in emissions over North America.

1. Introduction

In 1958 a monumental step was made to help us better understand the fate of fossil fuel CO_2 emitted into the atmosphere [*Keeling*, 1998] with the establishment of a CO_2 measurement site at 3400 m at Mauna Loa, HI (MLO). The seasonal cycle and interannual trends for CO_2 observed at this site and many other remote and urban sites have become instrumental in our understanding of the processes controlling CO_2 fluxes from the land and the ocean. MLO has particular significance because it was the first long-term continuous monitoring site for CO_2; measurements made there were well calibrated, and the site captured air that is representative of the variability in a large portion of the free troposphere. Since the first infrared analyzer was deployed at MLO, the global network that measures greenhouse gases has expanded considerably to include stations as far north as Barrow, Alaska, and Alert, Canada, and as far south as the South Pole. Initially, NOAA's Earth System Research Laboratory (ESRL) Global Greenhouse Gas Reference Network was limited to remote sites that would allow a better understanding of large-scale variability in greenhouse

gases with a focus on seasonal to interannual variability, as well as longitudinal and latitudinal variability [*Tans et al.*, 1989]. The present-day gradients measured in this network led to a better understanding of the role that ocean and land play in regulating atmospheric CO_2 both before [*Broecker and Peng*, 1992; *Heimann and Keeling*, 1986; *Keeling and Heimann*, 1986] and after [*Bousquet et al.*, 2000; *Gurney et al.*, 2004; *Jacobson et al.*, 2007; *Mikaloff Fletcher et al.*, 2006, 2007; *Tans et al.*, 1989, 1990] the industrial revolution. More recently, the Global Greenhouse Gas Reference Network has expanded to focus on continental processes because of the unexpectedly large uptake of CO_2 by terrestrial ecosystems in the temperate latitudes of the Northern Hemisphere [*Tans et al.*, 1990; *Ciais et al.*, 1995] and the large variability in uptake characteristic of land-based processes [e.g., *Andrews et al.*, 2014; *Gourdji et al.*, 2012; *Lauvaux et al.*, 2012].

In addition to the global network of ground stations, there have been several aircraft networks to monitor CO_2 and other greenhouse gases through the boundary layer, troposphere, and stratosphere. One of the first regular campaigns used commercial aircraft in the 1960s as a platform to sample CO_2 in air samples collected on flights between North America and Scandinavia and Japan [*Bolin and Bischof*, 1970]. More recent efforts have been made in Europe, Japan, and Australia, which feature both flask and in situ measurements on commercial aircraft [e.g., *Nakazawa et al.*, 1991, 1993; *Pearman and Beardsmore*, 1984; *Brenninkmeijer et al.*, 1999, 2007; *Machida et al.*, 2002, 2008; *Sasakawa et al.*, 2013; *Sawa et al.*, 2012]. While these measurements have been extremely valuable for stratospheric and high-tropospheric measurements of CO_2 and other greenhouse gases, measurements in the boundary layer and lower free troposphere have limitations for understanding fluxes to and from the biosphere owing to the requirement that the aircraft land at airports near large urban areas.

This study shows the compilation of over 10 years of CO_2 measurements from air samples collected using small aircraft in the NOAA/ESRL Global Greenhouse Gas Reference Network. Simultaneous observations of CO, CH_4, N_2O, and SF_6 are also considered here and provide insight into the processes driving climatological distributions of CO_2. The air samples are analyzed for a wide variety of compounds, as described in section 3. The data set includes observations from 22 sites spanning a large portion of the North American continent at sampling frequencies as high as twice per week. The resulting data have been instrumental for the evaluation of models [e.g., *Nakatsuka and Maksyutov*, 2009; *Stephens et al.*, 2007; *Yang et al.*, 2007; *Saeki et al.*, 2013; *Miller et al.*, 2012], satellite retrievals [e.g., *Maddy et al.*, 2008; *Xiong et al.*, 2008, 2010; *Yurganov et al.*, 2010; *Inoue et al.*, 2013; *Miyamoto et al.*, 2013] and solar-looking Fourier Transform Spectrometers (FTSs) [e.g., *Wunch et al.*, 2010]. This data set further forms the basis for a model-independent analysis of the net CO_2 sink in North America [*Crevoisier et al.*, 2010, 2006] in which the average monthly vertical distribution of CO_2 was estimated from 3 years of data. Using a Kriging method to interpolate the monthly observations between measurement sites, a four-dimensional data field was created by subtracting the deseasonalized trend measured for CO_2 at MLO from each aircraft observation. The subtraction allowed a multiyear data set to be distilled into a single "climatological" year of mole fraction differences from which mean continental flux of incoming and outgoing CO_2 could be differentiated to estimate net annual, monthly, and regional fluxes over North America. This study aims to build on that 2010 analysis with a detailed description of the NOAA/ESRL Global Greenhouse Gas Reference Network Aircraft Program, including its sites and sampling techniques, and to understand the drivers contributing to the climatological distributions of CO_2 with the help of information provided from the additional comeasured trace gases CO, CH_4, N_2O, and SF_6.

2. Methods

2.1. Sampling System

The backbone of the Aircraft Program is the programmable 12-flask sampling system used to collect air samples from small aircraft at different altitudes. The system consists of a programmable compressor package (PCP) and a flask package (12-pack), both designed by NOAA's Carbon Cycle Group. Here we give an overview of the basic programmable 12-pack sampling system.

The PCP is composed of two pumps connected in series. The first-stage pump (KNF Model N828 with aluminum head and Viton diaphragm) is designed to ensure flow rates of at least 5 L/min at 8000 m above sea level (masl) and 15 L/min at sea level. The second-stage pump (KNF Model N814 with aluminum head

and Viton diaphragm) is designed to ensure that samples can be reliably compressed to 40 psia (~275 kPa) at altitudes up to 8000 masl. The PCP is powered by a nickel-metal hydride (NiMH) rechargeable battery pack, which enables the pumps to fill up to four 12-packs (48 flasks) before recharging.

The 12-pack flask sampling unit is composed of twelve 0.7 L borosilicate glass flasks, a stainless-steel gas manifold system, and a data logging and control system. The 7.5 cm diameter cylindrical flasks have glass valves at each end and are stacked in two rows of six. A flexible stainless-steel manifold connects all of the flasks in parallel on the inlet side of the flasks. The valves at both ends of the flasks can be opened and closed with motor-driven valves. The valve mechanism is made up of a glass rod and a Teflon O-ring, which seals against a beveled glass valve seat when inserted into the valve body. The data logging and control system in the 12-pack provides the interface for controlling the sampling valves, storing a sampling plan, target flush volume, and fill pressure for the samples. The data logger also records the system status and a time stamp, actual sample flush volumes, and fill pressures during sampling. When GPS position, ambient temperature, pressure, and relative humidity are available from external sensors, the data logger also records these values at 10 s intervals.

A typical sampling site has one PCP and one or more 12-packs preprogrammed with a site-specific sampling plan that includes target altitudes for each sample. Before a typical flight, the system is first leak tested by flushing the internal flask manifold and then pressurizing to ~275 kPa. After 10 s the pressure is checked to ensure that there are no significant leaks in the tubing connecting the PCP and the 12-pack or within the manifold connecting all the individual flasks. The PCP is also connected to a pilot display, an alphanumeric LED display and toggle switch, which communicates target sampling altitudes to the pilot. Upon reaching each altitude, the pilot activates the toggle switch during level flight and waits until the sample is finished. Prior to collecting each sample, the inlet line and internal manifold are flushed with approximately 5 L (all flow rates and gas volumes are at STP) of ambient air. The valves on both ends of the selected sample flask are then opened and the flask is flushed with approximately 10 more liters of ambient air to displace the dry, low CO_2 (~330 μmol/mol), and zero CH_4 fill gas with which the flasks are shipped. The sample flush air is measured by a mass flow meter to ensure that at least 5 L of air passes through the manifold and flask before the downstream valve is closed and pressurization begins. Typically, pressurization of a flask takes 10 s and is monitored by an internal absolute pressure sensor. Assuming the lowest flow rate of 5 L/min, at 8000 m, and perfect mixing throughout the flask volume, >99% (5 e-folding times) of the flask will be flushed in the last 8.5 s of the flush cycle at the ambient pressure at 8000 m. An additional ~1.65 L of sample will be added once the downstream flask valve has been closed making the total sampling time under 18.5 s to collect >99% of the sample (assuming air in the 0.7 L flask is 35 kPa 8000 masl and is pressurized to 275 kPa, for a total of 2.2 L of sample air).

2.2. Analysis of Samples

The 12-pack is sent back to NOAA/ESRL in Boulder, CO, for analysis of as many as 55 trace gases, depending on the site. The gases fall into four broad categories including greenhouse gases, carbon isotopes, halocarbons, and hydrocarbons.

2.2.1. Greenhouse Gases (and CO and H_2)

Four greenhouse gases (CO_2, CH_4, N_2O, and SF_6,) as well as CO and H_2 are measured by one of two nearly identical Measurement of Atmospheric Gases Influencing Climate Change (MAGICC) automated analytical systems. The MAGICC systems consist of custom-made gas inlet systems, gas-specific analyzers, and system-control software. The gas inlet systems use a series of stream selection valves to select a specific flask, standard, or reference gas mixture. Before opening a flask, the flask manifold and sample inlet line are evacuated to 40 Pa to ensure that there is no residual gas in the manifold when the flask valve is opened. Once the flask valve is open, about 450 mL of sample gas pass through a cold trap, maintained at approximately −80°C for drying, and then passes into one of five trace-gas analyzers where dry-air mole fractions are measured. The following abbreviations are used: ppm = μmol mol^{-1}, ppb = nmol mol^{-1}, and ppt = pmol mol^{-1}. Standards used to calibrate instrument response are traceable to the respective World Meteorological Organization (WMO) mole fraction scale for each species (www.esrl.noaa.gov/gmd/ccl/index.html), where available. The first 100 mL of each air sample going into the MAGICC systems is used to flush the sample line and manifold after the evacuation. The second ~50 mL of sample flows into a gas

chromatograph (GC), which uses an electron capture detector to measure N_2O and SF_6 with a reproducibility of 0.4 ppb and 0.03 ppt, respectively. The third ~50 mL of sample is diverted to a second GC, with pulsed-discharge He ionization detection of H_2, with reproducibility of ±0.4 ppb [*Novelli et al.*, 2009]. Two instruments have historically been used to measure CO, a VURF (vacuum UV–resonance fluorescence) spectrometer with a reproducibility of ±0.4 ppb and a reduction gas analyzer (RGA) with reproducibility ~1 ppb [*Novelli et al.*, 1998]. Long-term comparison of the two systems shows the GC and fluorescence measurements agree within 1 ppb. A fourth ~50 mL aliquot of sample is diverted to a GC with flame-ionization detection of CH_4 with a reproducibility of ±1.2 ppb [*Dlugokencky et al.*, 1994]. Finally, a nondispersive infrared analyzer measures CO_2 in the next 100 mL of sample with a reproducibility of ±0.03 ppm [*Conway et al.*, 1994]. The reproducibility of each instrument is determined as the standard deviation of ~20 aliquots of natural air measured from a cylinder over a few hours, except for N_2O, which is determined as the standard deviation of the mean absolute difference of pairs of samples collected simultaneously in 2.2 L "network" flasks (pressurized to ~1.2 atm). Assessed the same way as the other species, reproducibility for N_2O is only ~0.2 ppb, but because average pair difference between flasks is ~0.4 ppb, we report the larger number as the reproducibility.

2.2.2. Halocarbons and Hydrocarbons

Approximately 35 halocarbons, hydrocarbons, and sulfur-containing trace gases have also been measured from flasks sampled at most of the Aircraft Program sites [e.g., *Montzka et al.*, 2007]. Although this study will not directly discuss the results of these measurements, they are an integral part of the data quality control. The gases are measured using a GC/mass spectrometric technique that requires a ~200 mL aliquot from each flask. Each sample is preconcentrated with a cryogenic trap consisting of an open-fused-silica tube (0.53 mm I.D.) maintained near liquid nitrogen temperatures. Analytes desorbed at ~110°C are then separated by a temperature-programmed GC column (30 m × 0.32 mm Gaspro), followed by detection with mass spectrometry to monitor compound-specific ion mass to charge ratios [*Montzka et al.*, 1993]. Flask sample responses are calibrated against whole-air working reference gases which, in turn, are calibrated with respect to primary standards prepared with gravimetric techniques (NOAA scales: CFC-11 on NOAA-1992, CFC-12 on NOAA-2001, HFC-134a on NOAA-1995, benzene on NOAA-2006, and all other hydrocarbons (besides methane) on NOAA-2008). Uncertainties for analyses reported here are $<5\%$.

2.2.3. Isotopic Ratios

A subset of 12-pack flasks is also analyzed for isotopic ratios of CO_2 at the University of Colorado Institute for Arctic and Alpine Research (INSTAAR) Stable Isotope Lab. An automated analysis system allows a ~450 mL sample to be analyzed for $^{13}C/^{12}C$ ratio of CO_2 (with 1σ reproducibility of ±0.01‰) and $^{18}O/^{16}O$ ratio of CO_2 (±0.03‰) [*Vaughn et al.*, 2004]. As with the MAGICC system, the manifold of each 12-pack is evacuated before the flask valve is opened. The whole air sample flows at 40 mL/min through one cold trap (−90°C) for drying and a second cold trap (−196°C) to extract CO_2 from whole air sample. The trap is then warmed and the extracted CO_2 is released into the bellows of a dual-inlet isotope ratio mass spectrometer (Isoprime, Elementar, Middlewich, UK) and compared against a "working" reference, which is pure CO_2 extracted from whole air collected at Niwot Ridge, CO. Working references have been linked to the VPDB-CO_2 scale by comparison with CO_2 evolved from carbonate primary standards [*Coplen*, 1995]. Up to four of the 12-packs can be automatically analyzed for isotopes in a 24 h period on the instrument.

A smaller subset of samples is measured for $^{14}C/^{12}C$ ratio of CO_2 [e.g., *Miller et al.*, 2012]. The high-precision measurements, reported as $\Delta^{14}CO_2$, are made through a combination of effort at the University of Colorado INSTAAR Laboratory for Accelerator Mass Spectrometer (AMS) Radiocarbon Preparation and Research (NSRL) and the Keck Accelerator Mass Spectrometry facility at the University of California at Irvine. The process begins by (a) extracting the CO_2 from whole air, using a cryogenic extraction system [*Turnbull et al.,* 2009], (b) reducing the CO_2 to elemental graphite over Fe catalyst with $Mg(ClO_4)_2$ to remove water, and (c) making the ^{14}C measurement with a high-count accelerator mass spectrometer (AMS) [*Turnbull et al.*, 2009]. Long-term reproducibility of $\Delta^{14}C$, based on repeated measurements from a target tank over nearly 10 years, is 1.8 per mil [*Lehman et al.*, 2013].

2.2.4. Data Archiving

An important feature of the 12-pack sampling system is that every 12-pack carries a log of sampling time, position, and, when available, temperature and relative humidity. This means that once the flask has been analyzed for greenhouse gases, carbon isotopes, halocarbons, and hydrocarbons, the measurement can be

Table 1. Long- and Short-Term Storage Test Average Offset and Standard Deviation of MAGGIC Gases in 12-Pack Flasks[a]

MAGICC Gas	Measurement Repeatability	Offset		Standard Deviation Between Flasks in Each 12-Pack	
		Short	Long	Short	Long
CO_2 (ppm)	0.03	−0.09 ± 0.05	−0.24 ± 0.08	0.04 ± 0.01	0.06 ± 0.03
CH_4 (ppb)	1.2	−0.15 ± 0.64	−0.0 ± 0.9	1.12 ± 0.38	1.06 ± 0.26
CO (ppb)	0.3	0.15 ± 1.4	1.34 ± 2.7	0.59 ± 0.42	0.8 ± 0.5
SF_6 (ppt)	0.03	−0.01 ± 0.04	−0.01 ± 0.04	0.04 ± 0.02	0.04 ± 0.04
H_2 (ppb)	0.4	−2.5 ± 6.1	0.50 ± 7.3	1.14 ± 0.67	1.8 ± 1.3
N_2O (ppb)	0.4	−0.39 ± 0.37	−0.8 ± 0.7	0.29 ± 0.15	0.3 ± 0.2

[a]All values in this table are given for 12-packs that have passed the basic CO_2 criteria that the standard deviation between the 12 flasks in a package in a short-term test is less than 0.055 ppm, with an offset less than 0.155 ppm, while the standard deviation between flasks in the long-term test is less than 0.155 ppm, with an offset less than 0.355 ppm. Offsets are based on differences between network flasks and 12-pack flasks. The uncertainty is a measure of standard deviation (1σ) of all storage tests.

immediately recorded in a central database and compared with trace gas measurements from surrounding sites and previous profiles.

At most sites, a global positioning system (GPS) receiver was not installed until late 2006, which meant that sampling time was derived from the clock inside individual 12-packs. To ensure that the 12-pack time closely matched the Greenwich Meridian Time (GMT), each 12-pack clock was reset before being shipped from Boulder to the site and checked again once it came back to Boulder. It was found that the internal battery of the data logger was sensitive to being stored at low temperatures (<0°C). In instances where the 12-pack clocks appeared to have drifted significantly (~6 min or more), times have been corrected manually based on the date and time of flight according to pilot records. In April of 2006 a system was initiated to record the difference in time between the 12-pack clock and GMT when the 12-pack was returned to Boulder after a sampling flight. Fewer than 1% of the 12-packs returned to Boulder had an offset greater than 6 min. The sample times on the data sheets are generally recorded after the flight and are not as accurate as those recorded automatically by the 12-pack. A switch to a new type of internal battery (Sanyo CR2450) and more reliance on GPS time has eliminated this time problem.

On flights where the GPS was not available, the ground position and altitudes have been inferred from the original sample plan specific to each site (Table 1). Unless otherwise noted, it is assumed that the original sampling plan for each site was followed. Because a typical profile is done by flying to the maximum altitude at the latitude and longitude of the sampling site followed by a slow downward spiral, leveling off at each sampling altitude, it is expected that most samples are taken within 0.1° of the site location (with the notable exception of PFA). GPS data collected more recently confirm this to be the case. It is also assumed that the pilots have used aircraft altimeters or pressure altitude to guide their sampling. Above 18,000 feet (5486 masl) the pressure altitude is based on the American Standard Atmosphere (ASA) [*Sissenwine et al.*, 1962], which assumes a constant sea level pressure of 101.325 kPa and a constant lapse rate of 6.5C/km up to 11,000 m. Below 5486 masl, the pressure altitude is determined using a local sea level pressure, which varies with time and space and assumes a constant lapse rate of 6.5C/km. The local sea level pressure is estimated by ground control based on a local pressure measurement and an altitude correction, which also assumes a lapse rate of 6.5 C/km down to sea level.

To correct pressure altitude to geopotential height when the GPS is not working or before it was available, we have utilized the Eta Data Assimilation System (EDAS, ftp://ftp.arl.noaa.gov/archives/edas40/readme.html) to derive the geopotential height. For each sample the ambient pressure is derived based on the target altitude and standard FAA protocol for altimeters. Using the EDAS data set (and the NCEP reanalysis for sites outside of EDAS domain), the ambient pressure is converted into geopotential height. Below 5486 masl, the local sea level pressure is also derived from local ground pressure from EDAS and local ground elevation. This method was tested using 2 years of data at the site over Briggsdale, Colorado (CAR). As expected, the pressure altitude was as much as 600 m below the GPS-measured geopotential altitude during the hottest summer days. The offset increased with altitude. Below 5486 masl the average offset between the pressure altitude and GPS was −80 ± 80 m (Figure 1a). After the correction based on EDAS pressures was made the offset was 8 ± 27 m, suggesting that the derived geopotential height was not significantly different from the measured (GPS) height (Figure 1b). Above 5486 masl, the mean offset between the pressure altitude and GPS was initially

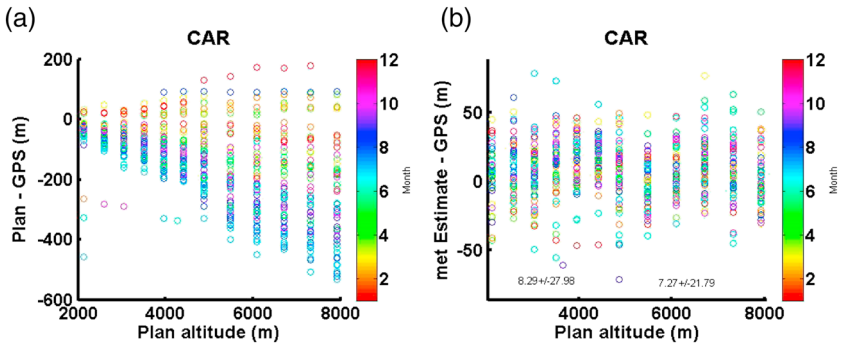

Figure 1. Comparison between sampling plan pressure altitudes and GPS position. (a) Difference before altimeter heights were corrected by reanalysis data and (b) difference (colored by month) in offset after corrections made by reanalysis data. Text illustrates the average offset between 2000 and 5400 m and between 5400 m and 8500 m.

220 ± 150 m. By using the meteorological reanalysis, the offset between estimated and measured altitude decreased to 7 ± 21 m. Similar trends have been documented when the GPS data can be compared with estimated altitude derived from pressure altitude and reanalysis data at other sites.

2.3. Quality Control

There are multiple sources of errors that can affect measurements and need to be assessed. Sources of error to the 12-pack flask measurement fall into three different categories: sampling errors, storage bias, and analysis errors.

2.3.1. Sampling Errors

Flow rate and time are monitored during sampling to determine how much air has been used to flush the manifold (>5 L) and each flask (>10 L) and to make sure that the target storage pressure (40 psia, 275 kPa) is reached. For most compressor packages these specifications are easily reached unless there is a leak in the system (e.g., a torn pump diaphragm or a break in the line between the compressor and flask package). However, there are many high-altitude samples that show no indication of contamination yet do not reach 275 kPa, which indicates that over time the PCP does not meet original specifications. For this reason, flask samples have been reviewed on a case-by-case basis to determine if there is obvious contamination due to sampling irregularities. In the sampling process, records of flows and instrument drift are examined to detect irregularities in the automated sample analysis. Because of cost and limited sampling resolution afforded by the 12-flask packages, duplicate sampling has not been performed on a regular basis, which means that we must rely on other indicators to detect contamination from the 12-flask system or aircraft.

For data presented here, there are two methods that have been used to identify potential contamination or leaks arising during the sampling process. The first approach is to bin the data by altitude and flag measurements whose residuals are at least three standard deviations from a smooth curve fit to the data [*Thoning et al.*, 1989]. The second approach for identifying potential contamination relies on a comparison of the multiple species that are measured in each sample. In particular, sample line leaks are typically identified by high CO from engine exhaust, tetrafluoroethane (Freon 134a, C_2H2F_4) and chlorodifluoromethane (HCFC-22,$CHClF_2$) from onboard air conditioning equipment, and/or bromochlorodifluoromethane (Halon 1211, $CBrClF_2$) from aircraft fire extinguishers. Because mass flow rates at higher altitudes are lower due to reduced pump performance, the influence of contamination and leaks increases at higher altitudes. When enhanced mole fractions of these specific compounds (CO, $C_2H_2F_4$, $CBrClF_2$) are measured, and not a broader general suite of gases indicative of general anthropogenic emissions, the MAGICC data are flagged to reflect possible contamination.

2.3.2. Storage Biases

Each flask is made with borosilicate glass that has been rinsed with phosphoric acid and distilled water and then dried at ~500C; this ensures that the inner surfaces of the flasks are clean initially before use. Once the flask package is assembled, it goes through both short-term (1–7 days) and long-term (~28 days) storage tests to identify leaks and possible contamination for gases measured on the MAGICC or hydrocarbon and

halocarbon systems. For a storage test, the 12-pack flasks and four low-pressure 2.2 L flasks used by the NOAA/ESRL Global Greenhouse Gas Reference Network ground sites ("network flasks") [*Conway et al.*, 1994] are all filled directly (i.e., not using the PCP) with dry air from a cylinder of natural air calibrated for the species of interest and stored in the laboratory before analysis. For each 12-pack, two network flasks are filled before and after successive filling of 12-pack flasks. The offset is defined as the difference between the 12-pack flasks and the network flasks to avoid biases due to fractionation of gases during the filling or a drift in the air sample. A summary of the storage test results can be found in Table 1. The standard deviation of the difference between the network flasks and the individual flasks in a 12-pack suggests that the 12-pack does add significant variability to the stated reproducibility of the MAGICC measurement for CO_2, CO, SF_6, and H_2. CH_4 and N_2O show relatively small offsets and variability relative to the measurement precision (Table 1). The storage tests of the 12-pack suggest that both CO_2 and N_2O are depleted with time relative to the NOAA network flasks.

Multiple storage tests over the last 5 years suggest that CO_2 and probably N_2O are diffusing through the Teflon O-ring seals at the end of each flask at the rate of about 0.007 ppm d^{-1} (for CO_2). This diffusion is driven, primarily, by the 175 kPa pressure gradient (which drives the gradient in the partial pressure of each gas) between the manifold and flask interior. Since both O_2 and N_2 diffuse more slowly across this pressure gradient, the net result is depletion in the CO_2 mole fraction over the time of storage. Data presented in this analysis have not been corrected for the storage bias given the fact that the average time lag between sampling and analysis for the 12-packs is less than 2 weeks, which would correspond to a correction of $\leq$0.1 ppm.

A limitation of the storage tests is that they use dry air, whereas sampled ambient air is not dried during aircraft sampling. The dry air storage tests show a small initial negative offset and the CO_2 mole fraction decreases further with additional storage time. Comparisons between 12-pack flasks and in situ instruments at either surface or aircraft sites indicate a bias in the opposite direction. In particular, *Andrews et al.* [2014] note apparent biases in certain individual samples in excess of 1 ppm and 0.36 ± 0.4 (1σ) on average in 12-pack flask measurements from the Boulder Atmospheric Observatory tall tower site during 2013. Similarly, *Biraud et al.* [2013] and *Karion et al.* [2013] observed biases in aircraft samples that although not significant (mean = 0.20 ± 0.36 and 0.20 ± 0.27 1σ, respectively) do suggest a similar bias. Comparisons over several years indicate that the mean biases are increasing with time [*Andrews et al.*, 2014]. Laboratory tests with humidified air suggest that high biases are not present in newly acid-washed and baked flasks but certain well-characterized flasks that have been used over longer periods show consistently high biases both in field comparisons and laboratory tests. Comparisons with in situ measurements following a recent change in 12-flask sampling protocol at surface sites show that prefilling and pressurizing flasks with ambient air to 275 kPa immediately before sampling, to condition the wall of the flask and the valve, significantly diminishes the observed differences between flask samples and in situ measurements [*Andrews et al.*, 2014]. Because these biases have apparently increased over time [*Andrews et al.*, 2014] and are not consistent among different flasks, the potential bias is hard to quantify. Atmospheric variability also complicates individual comparisons with in situ instruments, so dedicated testing under controlled conditions will be required to characterize current biases for individual flasks. Starting in August of 2014 all aircraft 12-pack flasks have been prefilled and pressurized with ambient air in accordance with the protocol that has been demonstrated to improve flask versus in situ comparisons at ground sites. Given that this analysis is looking at broad scale changes in CO_2 ($>$1 ppm), these potential biases will not significantly affect the results discussed in this study.

Biases in undried samples of CO, CH_4, H_2, SF_6, and N_2O are not observed within the measurement repeatability of the dry air test flasks described above (Table 1). In situ comparisons are available for CO and CH_4 [*Andrews et al.*, 2014; *Karion et al.*, 2013] and agree to within the uncertainty of the measurements.

2.3.3. Analysis Errors

The final category in the quality control of 12-pack flasks measurements is the errors during sample analysis which are identified based on target gas and standard gas drift and reproducibility during analysis of flasks. In many cases abnormal initial pressure or humidity in the flask or low flow rates, operating temperatures, and pressures are noted to identify potential sources of error that may not be accounted in the standards and target gases which are dry and introduced into the analysis system with slightly different plumbing configurations.

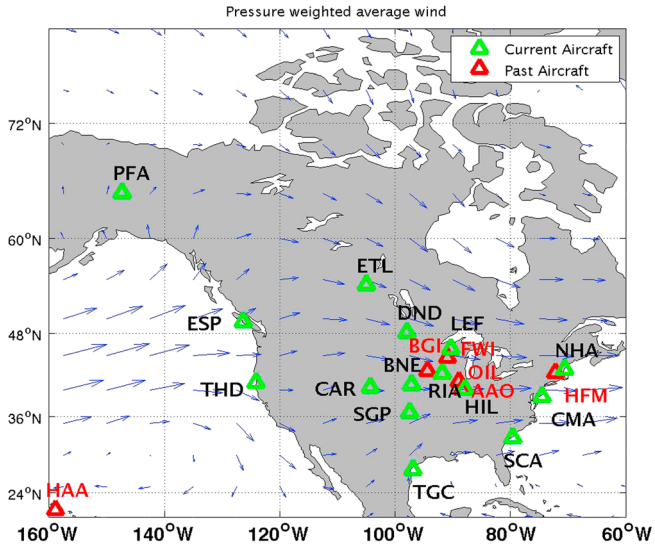

Figure 2. Aircraft measurement locations in the NOAA/ESRL Global Greenhouse Gas Reference Network. Current (2014, green) and past (red) sites where 12-flask samples are taken The single Southern Hemisphere site, Rarotonga, Cook Islands (RTA), has been omitted. Blue vectors represent annual mean wind vectors vertically weighted by relative pressure at each altitude bin from ground to ~8000 masl.

2.4. Site Descriptions

This study will focus on data from samples collected at 22 sites (Figure 2) in North America from 1 January 2004 to 1 January 2014. This includes 16 sites that, as of 1 January 2014, were still in operation and six sites that have been discontinued during this 10 year period (Table 2). A variety of factors determines the sampling frequency, including partnerships, funding availability, and pilot reliability.

Of the 22 sites, all but four include samples collected up to altitudes between 7500 masl and 12,000 masl. The average time interval between samples has varied over the course of the last 10 years with some sites being sampled every 2–3 days at times while other sites can be sampled as little as once every two months. At most sites, all 12 samples are taken at different altitudes with closer spacing at altitudes (~500 m) near the boundary layer and wider spacing in altitudes (~1000 m) above 6000 masl.

2.5. Data Reduction

Because it is easily accessible, available at a high time resolution, and relatively unaffected by local variability, a large fraction of the analysis presented in this study will use the Mauna Loa (MLO) data set for CO_2, CH_4, CO, SF_6, and N_2O as a reference to understand the large-scale temporal and spatial gradients observed between each aircraft site.

To emphasize different aspects of the NOAA/ESRL Global Greenhouse Gas Reference Network Aircraft Program observations, methods described by *Thoning et al.* [1989] are used to fit both a deseasonalized trend and a seasonal trend to MLO. The MLO trends are then used to detrend the Aircraft Program data. These trends are established by fitting the MLO data to a polynomial trend and series of harmonics using

$$x(t) = a + bt + ct^2 + \sum_{i=1}^{4} d_i \sin\omega_i t + e_i \cos\omega_i t \quad (1)$$

where ω_ι is equal to $2\pi i$ ($i = 1$ to 4) and t is time in years. A least squares fit of equation (1) allows the time series to be detrended with coefficients a, b, and c and provides the amplitude [sqrt($d_i^2 + e_i^2$)] of each harmonic ($i = 365$, 182, 122, and 91 days) over the whole MLO time series. By smoothing the residuals of the fit to equation (1) with a filter having a full width at half maximum (FWHM) in the time domain as described by *Thoning et al.*, 1989] of ~400 days, it is possible to derive a deseasonalized trend by adding this smoothed function to the original third-order polynomial fitted to the data (Figure 3). The resulting deseasonalized trend line effectively captures interannual variations with a time scale longer than a year that would not be captured by the second-order polynomial fit of the MLO data.

3. Results

This section has four parts each of which builds on the preceding ones to illustrate the main processes contributing to the seasonal cycle at each aircraft site. In the first section the aggregate of all the data collected by the NOAA/ESRL Global Greenhouse Gas Reference Network Aircraft Program relative to MLO is presented to illustrate basic trends and gradients between samples collected at different altitudes. In the

Table 2. NOAA/ESRL Carbon Cycle Aircraft Network Site Locations

Code	Name	Latitude	Longitude	First Sample Date	Status	Bottom Altitude (masl)	Top Altitude (masl)	Days Between Samples
AAO	Airborne Aerosol Observing	40.10	−88.40	6/7/2006	Terminated	396	4572	4
BGI	Bradgate, Iowa	42.82	−94.41	9/13/2004	Terminated	610	7620	14
BNE	Beaver Crossing, Nebraska	40.80	−97.18	9/15/2004	Terminated	599	8120	27
CAR	Briggsdale, Colorado	40.37	−104.30	11/9/1992	Ongoing	2101	8410	17
CMA	Cape May, New Jersey	38.83	−74.32	8/17/2005	Ongoing	305	7620	17
DND	Dahlen, North Dakota	48.38	−99.00	9/21/2004	Ongoing	518	8131	33
ESP	Estevan Point, British Columbia	49.58	−126.37	11/22/2002	Ongoing	152	5695	25
ETL	East Trout Lake, Saskatchewan	54.35	−104.98	10/15/2005	Ongoing	904	7228	34
FWI	Fairchild, Wisconsin	44.66	−90.96	9/20/2004	Terminated	610	7620	14
HAA	Molokai Island, Hawaii	21.23	−158.95	5/31/1999	Terminated	300	7620	21
HFM	Harvard Forest, Massachusetts	42.54	−72.17	11/11/1999	Terminated	610	7620	19
HIL	Homer, Illinois	40.07	−87.91	9/16/2004	Ongoing	609	8059	30
LEF	Park Falls, Wisconsin	45.95	−90.27	4/10/1998	Ongoing	549	5060	14
NHA	Worcester, Massachusetts	42.95	−70.63	9/12/2003	Ongoing	299	7620	16
OIL	Oglesby, Illinois	41.28	−88.94	9/16/2004	Terminated	610	7620	12
PFA	Poker Flat, Alaska	65.07	−147.29	6/27/1999	Ongoing	283	7604	21
RTA	Rarotonga, Cook Islands	21.25	159.83	4/16/2000	Ongoing	100	6528	33
SCA	Charleston, South Carolina	32.77	−79.55	8/22/2003	Ongoing	282	12802	20
SGP	Southern Great Plains, Oklahoma	36.80	−97.50	9/17/2002	Ongoing	172	5330	6
TGC	Sinton, Texas	27.73	−96.86	9/9/2003	Ongoing	265	8107	49
THD	Trinidad Head, California	41.05	−124.15	9/2/2003	Ongoing	291	7953	37
WBI	West Branch, Iowa	41.73	−91.35	9/14/2004	Ongoing	572	8073	71

second section the seasonal cycle, the vertical gradients, and the relative timing of the seasonal cycle are examined with respect to the location of each site. In the third section the basic mass transport of each region is analyzed to better understand the vertical and horizontal variability in the net horizontal mass flux of CO_2 as air move across the North American continent, which is presented in the final section.

3.1. Seasonal and Temporal Trends of Aircraft Data Relative to Mauna Loa

For CO_2 the root mean squared (RMS) deviation of MLO flask measurements from the MLO seasonal trend is 0.39 ppm, which is 6% of the peak to peak amplitude of the seasonal cycle. For CO and CH_4 the RMS deviation of data from the calculated seasonal trend is 10 ppb and 9 ppb, which is 21% and 30% of the estimated seasonal amplitude, respectively. SF_6 and N_2O seasonal cycles at MLO are not as easily discernible from the deseasonalized trend given that the RMS deviation has about the same magnitude as the peak to peak amplitude of the seasonal cycle. Although this mostly driven by the long lifetime of N_2O and SF_6, this may also be an artifact of relatively low signal-to-noise ratio in the measurement of these two species and/or a function of the relatively high spatial variability compared to seasonal changes in mole fraction due to variability in transport and emissions. With the exception of CH_4 and CO, the combination of the seasonal and deseasonalized trends at MLO provides a good baseline for measurements from aircraft sites throughout North America. Because of very large sources of CH_4 and CO at low latitudes, subtle changes in transport of emissions in these regions can significantly affect observations at MLO. This study takes advantage of the seasonal and deseasonalized trends at MLO to understand the accumulated influence of flux and mixing at each NOAA/ESRL Global Greenhouse Gas Reference Network Aircraft Program site relative to what is measured at MLO.

The value of the comparison of MLO to all the aircraft sites is best illustrated by overlaying all CO_2, CH_4, CO, SF_6, and N_2O measurements made at MLO over all aircraft measurements (Figure 4). For CO_2 samples collected from the NOAA/ESRL Global Greenhouse Gas Reference Network Aircraft Program, there are several conclusions that can be made. First, MLO sets a strong lower limit of CO_2 observations in the winter and a loose upper limit in early summer. Second, MLO shows a significant temporal lag relative to the boundary layer values at other sites in North America. The implications of these two observations are that seasonal cycles at MLO are a lagged and damped response to boundary layer drawdown of CO_2 in the summer and enhancement in the winter as pointed out by *Thoning et al.* [1989].

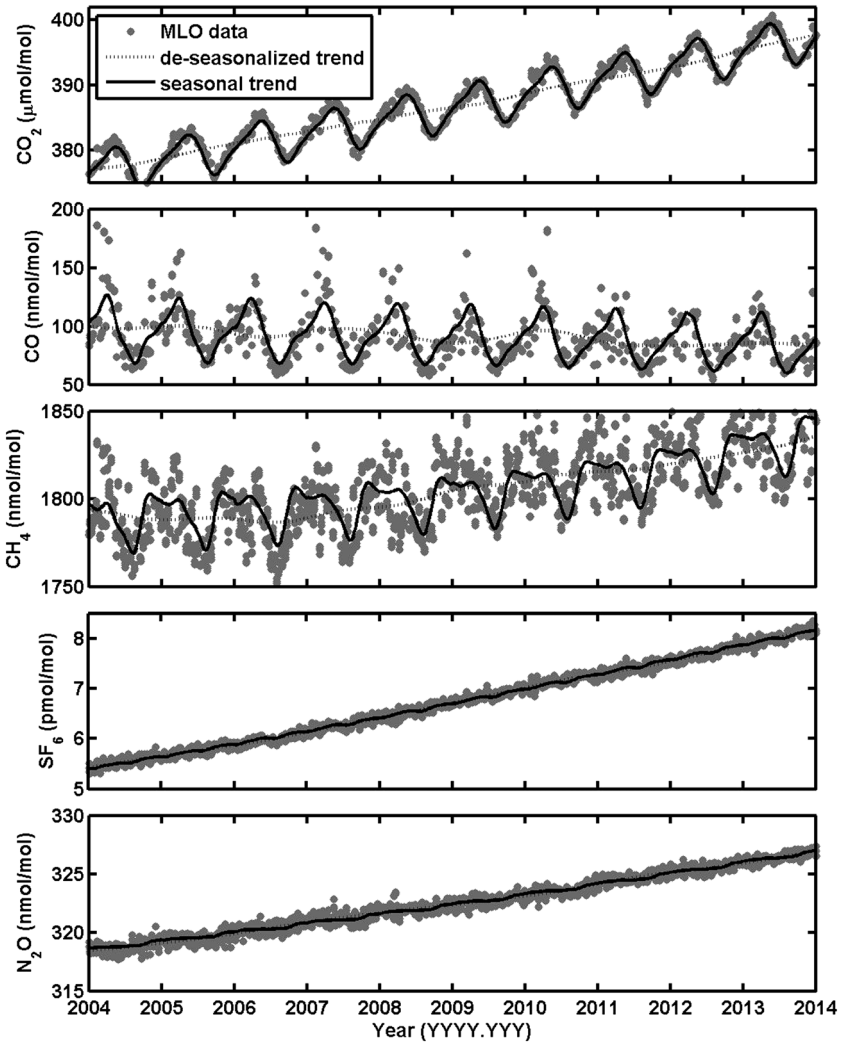

Figure 3. Yearly and seasonal trends in CO_2, CO, CH_4, SF_6, and N_2O at Mauna Loa (MLO). Solid black line illustrates the seasonal trend, and the dotted line illustrates the deseasonalized trend in the data [*Thoning et al.*, 1989].

For CH_4, CO, and SF_6, MLO provides a clear lower boundary for all sites except RTA, which is expected since RTA is in the Southern Hemisphere and most of the emissions sources for these gases are located in the Northern Hemisphere (north of MLO) and significantly higher mole fractions are measured in the Northern Hemisphere. For CH_4 and CO, the meridional gradient between MLO and the other North American sites is enhanced by the oxidation reaction with the OH radical, which has a higher abundance at low latitudes [*Dlugokencky et al.*, 1997; *Montzka et al.*, 2000; *Naik et al.*, 2013; *Patra et al.*, 2014].

N_2O observations at MLO provide an important reference point for its growth rate. High outliers above the MLO observations are generated from high boundary layer N_2O mole fractions observed during the springtime in the midcontinent, consistent with studies that suggest that the agriculture is a largest source of N_2O [e.g., *Syakila and Kroeze*, 2011]. Observations of N_2O mole fraction below those observed at MLO in the free troposphere are consistent with model results that show a significant transport of N_2O-depleted stratospheric air into the free troposphere at high northern latitudes [*Thompson et al.*, 2014].

It is important to note the boundary layer enhancements for each species (dark gray dots, Figure 4). While the uptake of CO_2 during spring and summer causes depletion in the boundary layer, data for all other gases suggest that boundary layer sources are fairly continuous throughout the year.

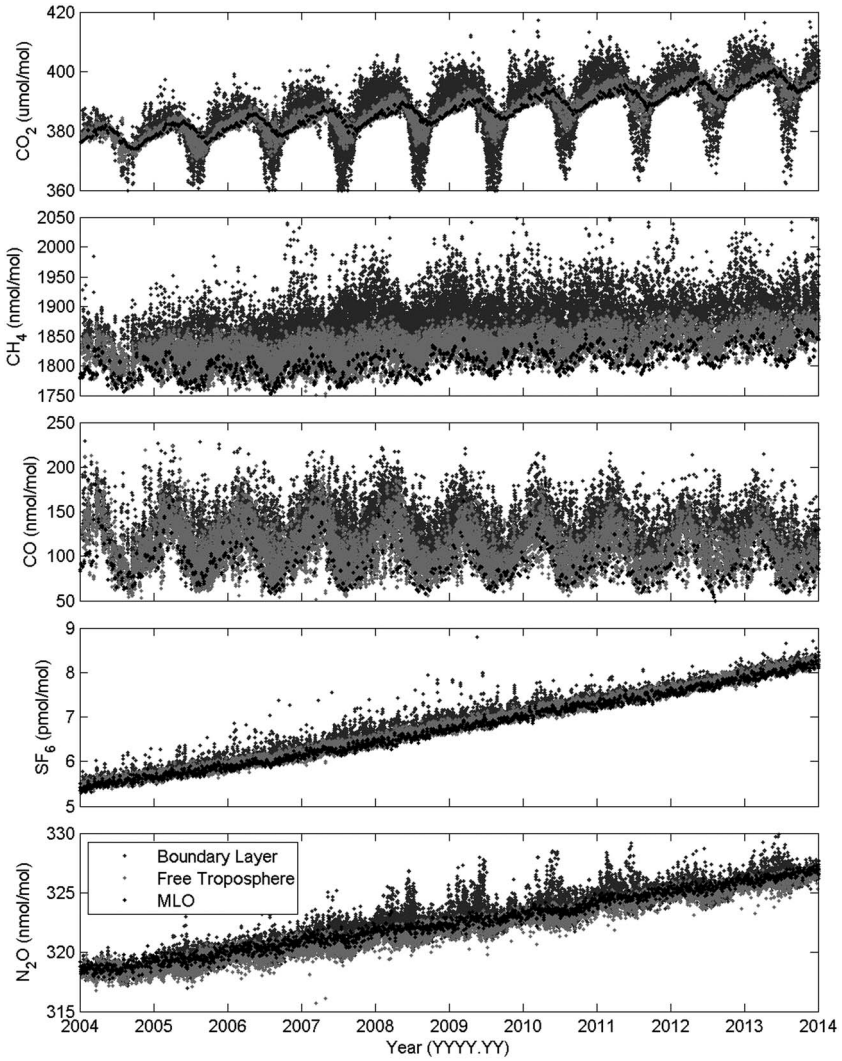

Figure 4. CO_2, CH_4, CO, SF_6, and N_2O observations from aircraft measurements in the NOAA/ESRL Global Greenhouse Gas Reference Network (all sites). The boundary layer is defined by observations below 3500 masl (dark gray), and the free troposphere observations are made above 3500 m (light gray). Observations from Mauna Loa (MLO) are shown in black.

3.2. Spatial and Temporal Patterns in Seasonal Cycle

To show the spatial and temporal patterns in CO_2, CH_4, CO, N_2O, and SF_6 over an annual cycle, the data from each site have been aggregated into a single year by subtracting the mole fraction estimated from the MLO deseasonalized trend for each species and binning the deviation by month and altitude. The resulting monthly deviation from the deseasonalized trend provides an annual climatology. Although the focus of this paper is on the CO_2 profiles from the NOAA/ESRL Global Greenhouse Gas Reference Network Aircraft Program, the spatial and seasonal distributions of CH_4, CO, N_2O, and SF_6 are also considered to better understand processes controlling the gradients observed for CO_2.

3.2.1. Spatial Representativeness of the Seasonal Climatology

By design, the seasonal climatology of CO_2, CH_4, CO, N_2O, and SF_6 for each aircraft site emphasizes large-scale features in both space and time (Figures 5–9). Temporal smoothing is achieved by binning the data (as deviations from MLO) by month and altitude. Most sites have been in operation for more than 6 years and have at least eight measurements per month in each altitude bin, so that anomalies from point sources outside the typical footprint of a site, convective events, or fronts are typically averaged out. Spatial smoothing is achieved because a large portion of the air captured in each vertical profile has not been recently ($<$3d) influenced by boundary layer processes, thus providing time for smoothing of the signal. From this perspective it is not surprising that NHA

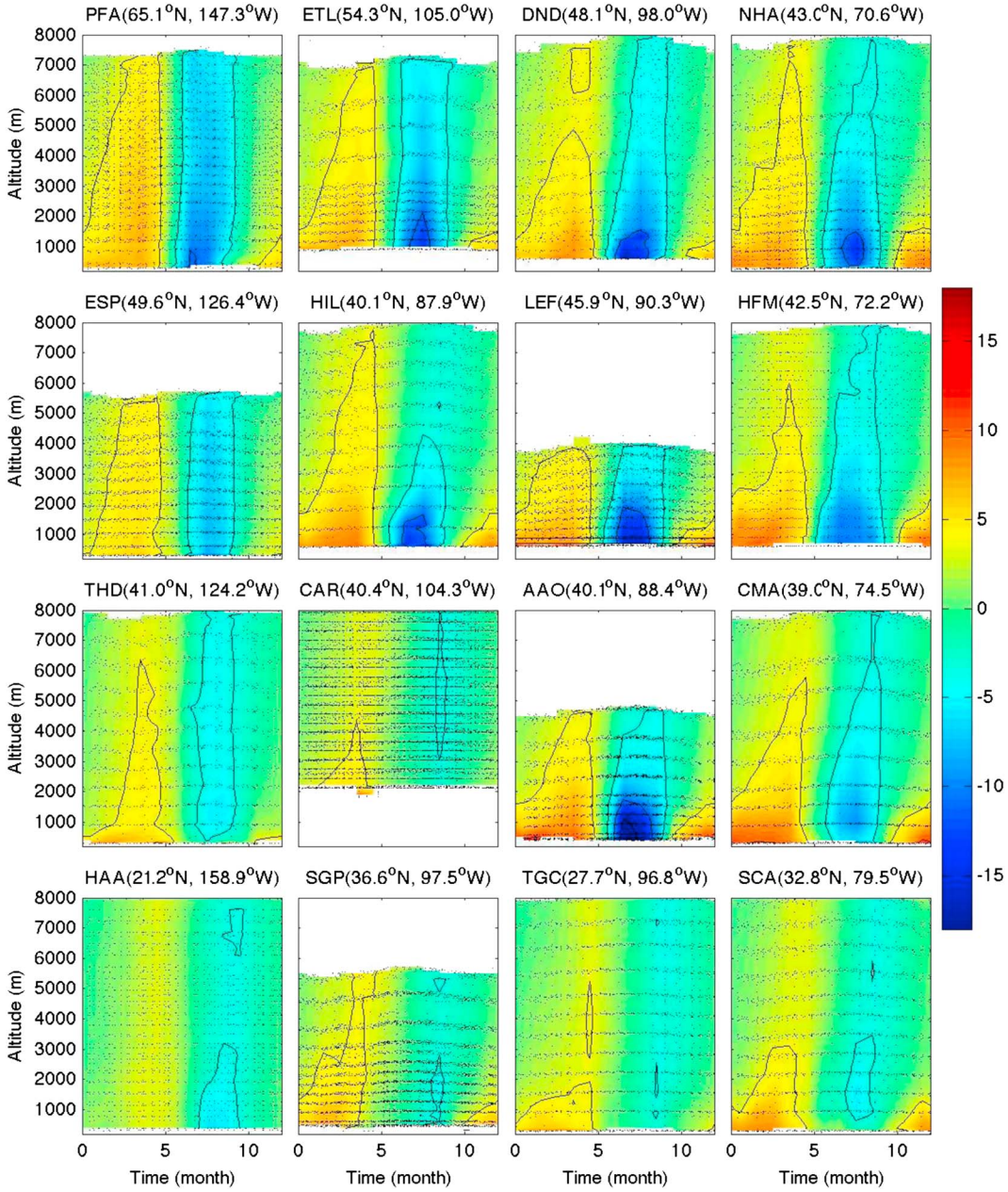

Figure 5. Annual climatology of CO_2 from 16 sites in the NOAA/ESRL Global Greenhouse Gas Reference Network Aircraft Program. Each panel shows the deviation of CO_2 mole fraction (ppm) from the deseasonalized trend at MLO. The black dots illustrate sample location, and the color matrix is a compilation of vertical profile measurements binned in monthly increments.

and HFM or AAO, LEF, and HIL have similar annual climatologies for CO_2 (Figure 5). The CO_2 climatologies at HFM and NHA, which are separated by more than 475 km, demonstrate the robustness of the temporal and spatial smoothing by their similarity. Both sites share very similar distributions of CO_2 with large summertime drawdowns in boundary layer mole fraction followed by large increases in wintertime CO_2 from accumulation of fossil fuel emissions and ecosystem respiration in air masses traveling across the continent. The CO_2 seasonal cycles at these two sites look almost identical despite the fact that their sampling frequencies and duration of the time series analyzed are quite different. While NHA has been consistently sampled from September 2003 through present day, sampling at HFM started in November 1999 and ended in November 2007. The methane and nitrous oxide and to some extent the CO distributions are also similar at these two sites (Figures 6, 7, and 9), but the annual climatology of SF_6 between the two sites shows notable differences

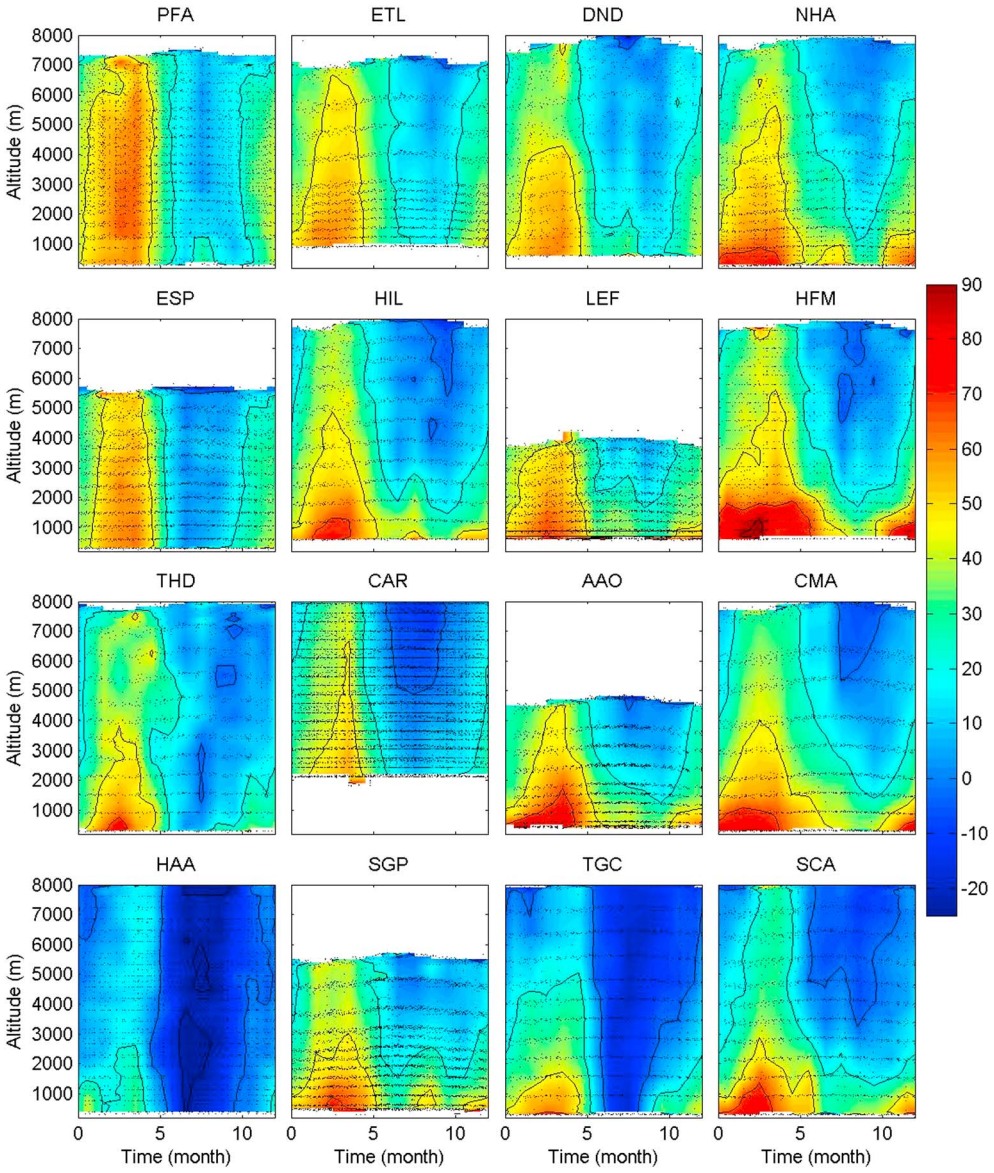

Figure 6. Annual climatology of CO from 16 sites in the NOAA/ESRL Aircraft Network. Each panel shows the deviation of CO mole fraction (ppb) from the deseasonalized trend at MLO. The black dots illustrate sample location, and the color matrix is a compilation of vertical profile measurements binned in monthly increments.

(Figure 8). It is clear from boundary layer enhancements of SF_6 and CO at HFM that there are local point sources of SF_6 and CO captured in aircraft samples that are not easily detectable in the samples collected at NHA. While sources for CO can be very broad and diffuse, SF_6 (which is typically emitted from electrical substations and a few other locations) tends to have a more localized enhancement in the boundary layer. Because the seasonal cycle of CO_2 is dominated by processes forced by large-scale drivers, ecosystem respiration during the winter and ecosystem net uptake (photosynthesis minus respiration) during the summer, a large spatial scale to the seasonal cycle is expected. Between the two extremes of CO_2 (with a large natural signal and fewer point sources) and SF_6 (with only point sources) lie CH_4, N_2O, and CO, where site-to-site variation is less dependent on local sources and more on regional sources than observed for SF_6.

3.2.2. Spatial and Temporal Trends in CO_2

Although there is a wealth of information about sinks and sources for CH_4, CO, N_2O, and SF_6 that can be extracted from the seasonal climatologies, the analysis in this study is primarily focused on understanding the sources of variability in the CO_2 annual climatology (Figure 5). As expected, the seasonal cycle due to

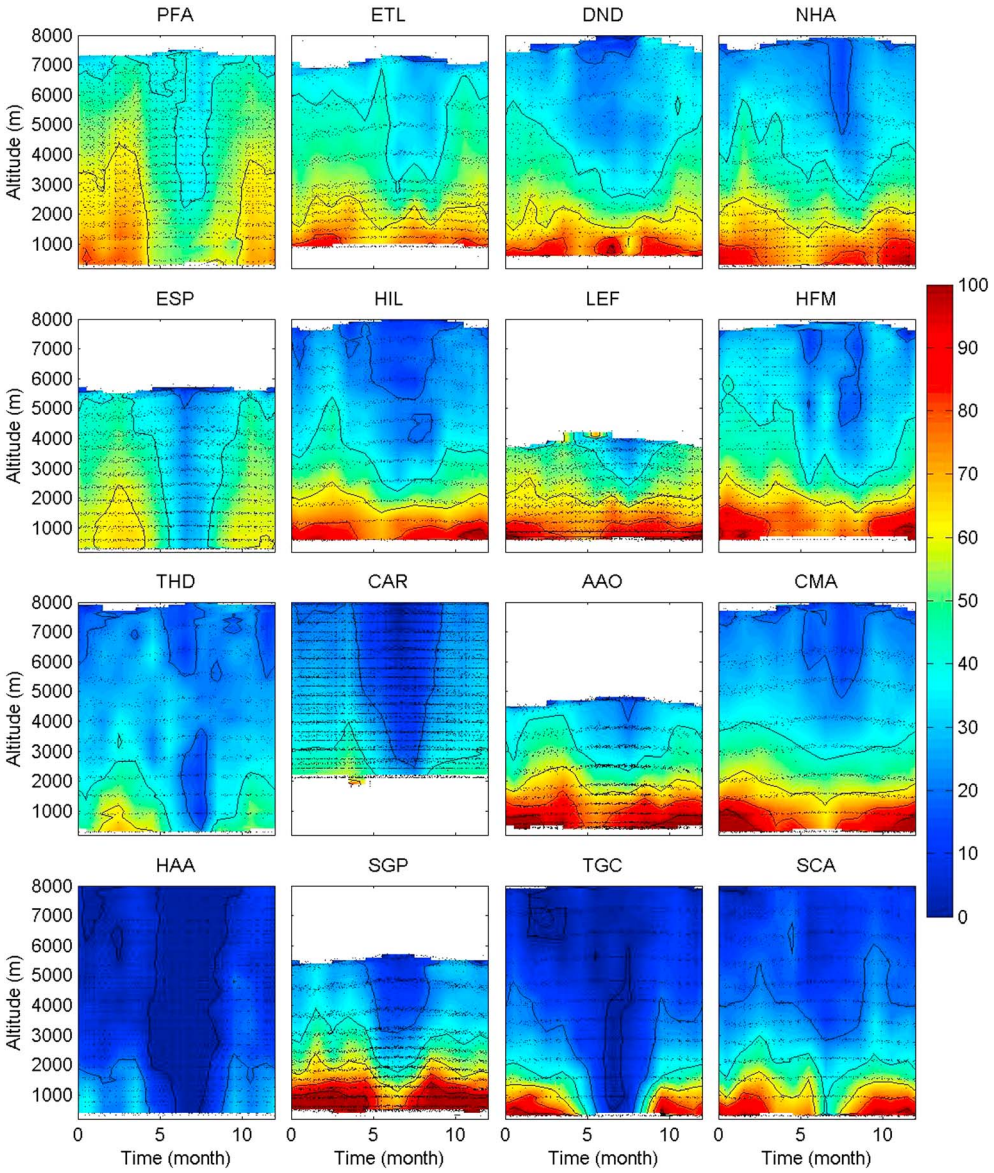

Figure 7. Annual climatology of CH_4 from 16 sites in the NOAA/ESRL Aircraft Network. Each panel shows the deviation of CH_4 mole fraction (ppb) from the deseasonalized trend at MLO. The black dots illustrate sample location, and the color matrix is a compilation of vertical profile measurements binned in monthly increments.

land-based respiration and photosynthesis is the most obvious source of variability up to 8000 masl. At the West-Coast sites the column is relatively well-mixed with respect to CO_2, but at the more Mid-West and East-Coast sites the seasonal cycle becomes more pronounced in the boundary layer. This is particularly true for sites in the Mid-West where summertime productivity dramatically decreases the boundary layer CO_2 mole fractions (Figure 10). Although not as dramatic in the near surface, the column-integrated seasonal cycles suggest that sites in the northeast show the most dramatic seasonal change. Similarly, measurements at PFA show that the vertical mixing has distributed the seasonal change in CO_2 throughout the column above 8000 masl (Figure 5 and Table 3). It also should be noted that while the northeastern sites (NHA and HFM) show large column-integrated changes in CO_2, the summertime CO_2 minimum in the boundary layer is not as dramatic as that observed at the Mid-West sites (LEF, AAO, HIL, Figure 5). *Miller et al.* [2012] show through analysis of $^{14}CO_2$ measurements made at NHA and CMA that summertime CO_2 is enriched by an average of 2.2 ppm of fossil fuel CO_2 in the lower 2.5 km (relative to air at ~4 km). The relative increase in CO_2 in the wintertime boundary layer of the northeast sites also

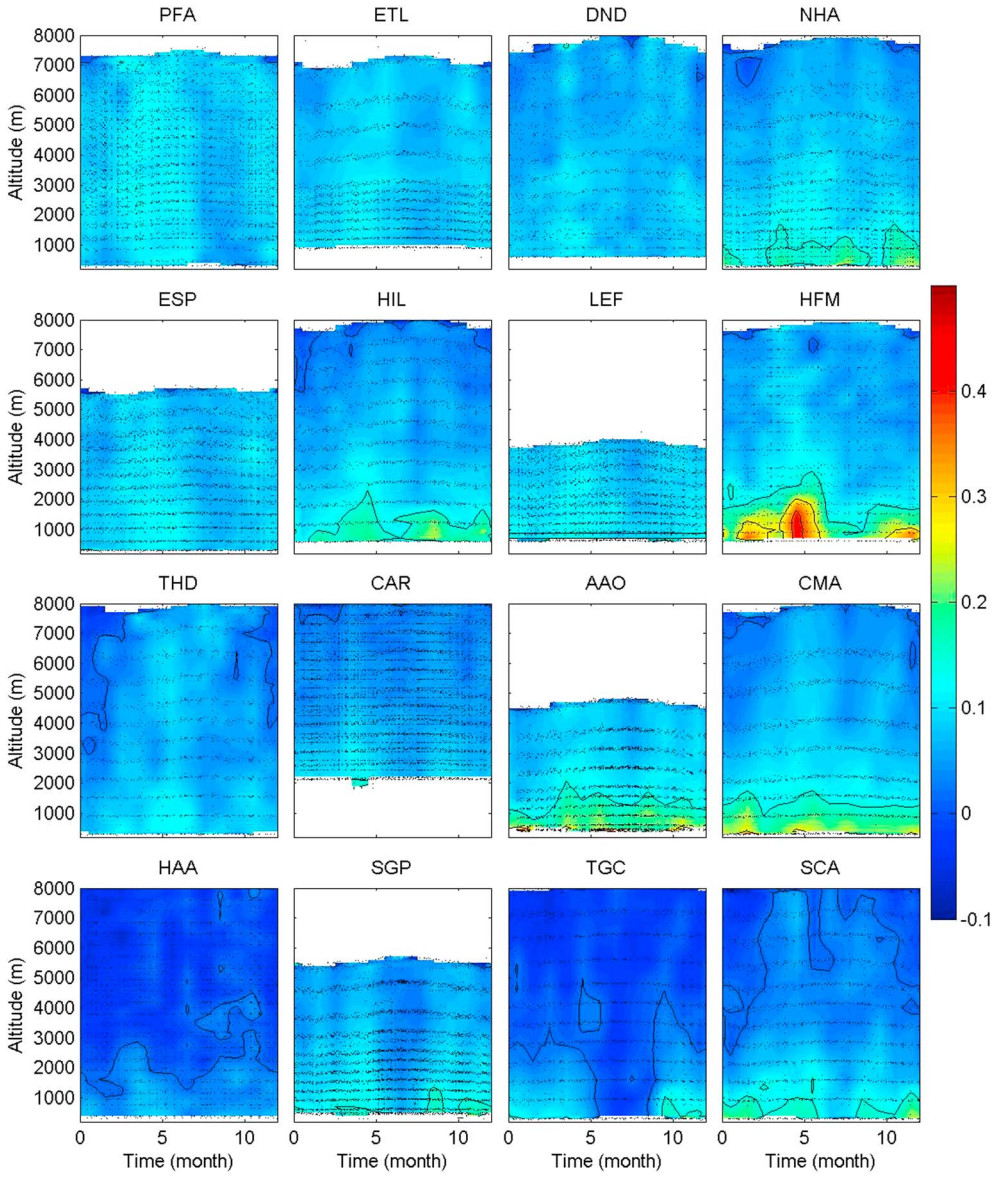

Figure 8. Annual climatology of SF_6 from 16 sites in the NOAA/ESRL Aircraft Network. Each panel shows the deviation of SF_6 mole fraction (ppt) from the deseasonalized trend at MLO. The black dots illustrate sample location, and the color matrix is a compilation of vertical profile measurements binned in monthly increments.

suggests a net accumulation of both fossil fuel and biologically produced CO_2 as air masses move north and east across the continent. The $\Delta^{14}C$ data at NHA and CMA show that the wintertime CO_2 enrichment is about 50% due to respiration. This will be more obvious in our analysis of CO_2 mass transport (below).

In the same way that the magnitude of the seasonal cycle increases from west to east in the continental United States, there is also a large increase in variability in boundary layer mole fractions within each month (Figure 11). This result is expected as fronts move across regions with increasingly higher vertical gradients in CO_2; there is a tendency for vertical mixing from convective storms to erase vertical gradients quickly, causing the observed temporal variability in the boundary layer mole fractions. More vigorous mixing and higher fluxes during the summer months is suggested by higher variability within each summer month.

3.2.3. Using MLO as an Indicator of the Free Troposphere

A slightly different perspective on the spatial distribution of the seasonal cycle of CO_2 profiles can be gained by looking at the deviation of each CO_2 mole fraction measurement throughout the profile with respect to the seasonal trend at MLO (Figure 12) instead of the deseasonalized trend (Figures 5–9). This provides a

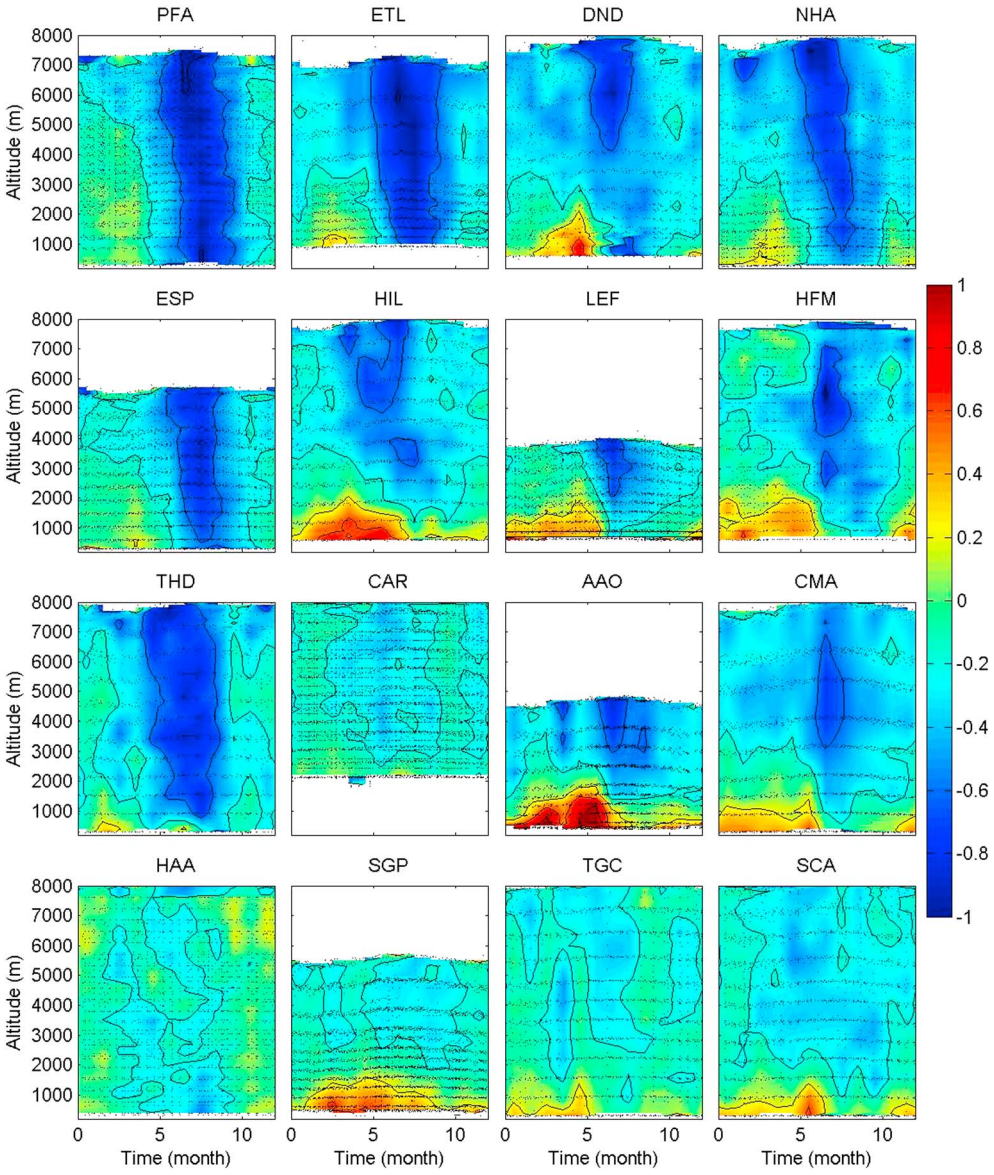

Figure 9. Annual climatology of N_2O from 16 sites in the NOAA/ESRL Aircraft Network. Each panel shows the deviation of N_2O mole fraction (ppb) from the deseasonalized trend at MLO. The black dots illustrate sample location, and the color matrix is a compilation of vertical profile measurements binned in monthly increments.

better understanding of the spatial gradients (both horizontal and vertical) that exist between MLO and other sites because the effects of the seasonal cycle at MLO have been eliminated. The immediate result is an understanding of how measurements at each profile site differ from MLO. An examination of HAA, which is located 40 km from MLO, provides a measure of how local variability at the different sites might add noise to this analysis. Local variability in the boundary layer can cause as much as 4 ppm difference between what is measured at HAA and at MLO (3400 masl). Above the boundary layer the variability is ±1.5 ppm (1σ) with a small offset, with HAA slightly lower than MLO in the summer and higher than MLO in the winter.

Moving northeastward to THD, ESP, and PFA in western North America, there are significant differences from the seasonal trend of MLO. There significant differences not only in the boundary layer but also throughout the profile up to 8000 masl. This is particularly true at PFA where both summertime (July–September) and wintertime (October–March) are significantly different from MLO. PFA is particularly remarkable because the offset from MLO is relatively constant from the boundary layer to the topmost samples (~8000 masl)

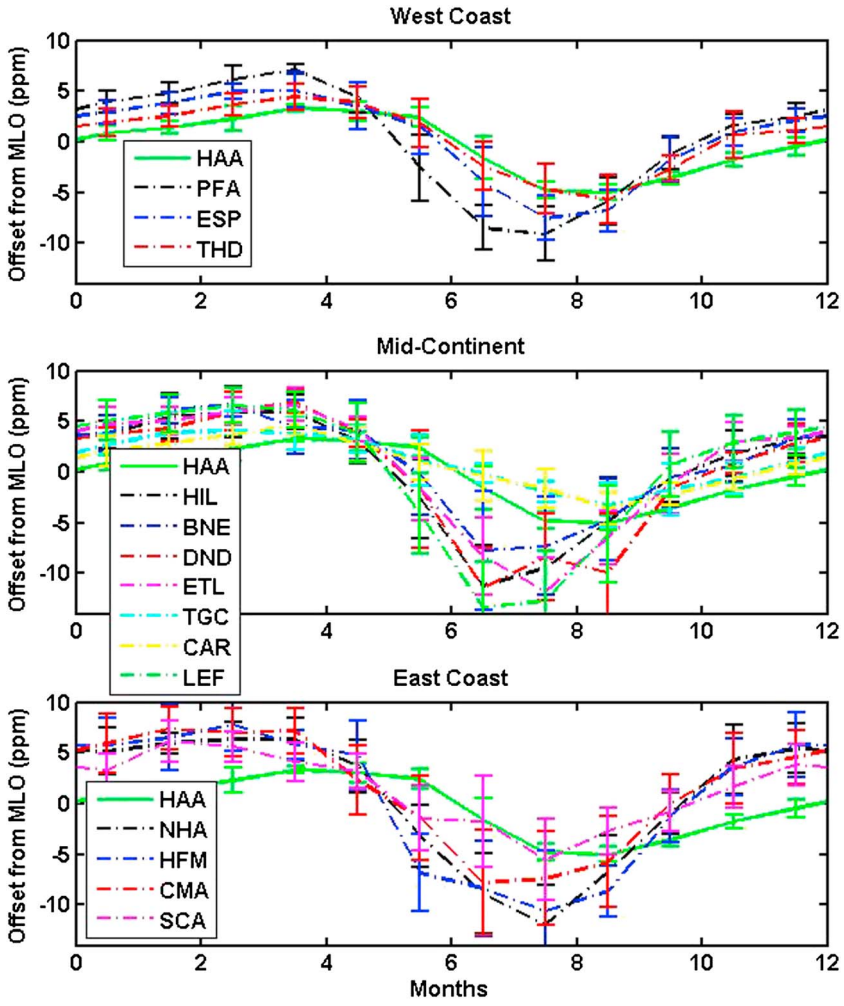

Figure 10. Seasonal cycle of boundary layer offset from the deseasonalized trend at MLO for west continental, midcontinental, and east continental regions of North America. The boundary layer measurements have been defined by measurements contained in the lower 150 mbar of the climatology (Figure 5). The mean values are a reflection of the data corrected for the trend at MLO and binned into monthly intervals; error bars indicate the 1σ standard deviation.

suggesting a very well-mixed column. A large part of the offset can be explained by the fact that the summertime minimum in CO_2 precedes the MLO summertime minimum by ~1.5 months (Table 3). This offset closely resembles the minimum in CO_2 that is observed in the boundary layer of the midcontinent and northeastern sites suggesting that similar processes are contributing to the summertime minimum at PFA. The difference between these west coast sites and the midcontinent sites is that the offsets from MLO are consistent vertically throughout the CO_2 profiles; this suggests that as the air masses are moving across the Pacific vertical mixing processes are propagating boundary layer depletions (in summer) and enhancements (in winter) throughout the vertical column. In support of the efficient vertical transport mixing CO_2, it is worth noting the absence of a vertical gradient between the boundary layer and free troposphere for CO, CH_4, N_2O, and SF_6 at THD, ESP, and PFA. This is not the case for the Mid-West and East Coast sites where vertical transport, surface-to-air fluxes into the boundary layer, and chemical breakdown or dilution in the free troposphere all play a major role in controlling the vertical gradients above the boundary layer (Figures 6–9).

Moving eastward along the northern part of the survey region, both ETL and DND also show offsets from the seasonal fit of MLO throughout the vertical profiles (Figure 12) suggesting that whatever processes influence the free troposphere air (>4000 masl) on the West Coast sites continue to influence northern sites further inland and that regional influences on high-altitude samples are relatively weak. At sites farther south

Table 3. Average Column (0–8000 masl) Seasonal Cycle and Vertical Gradients for CO_2[a]

Site	Lag (years)	Amplitude (ppm)	Minimum Gradient (ppm/km)	Min (month)	Maximum Gradient (ppm/km)	Max (month)	Region
AAO[b]	−0.16 ± 0.01	13.6 ± 4.1	−2.0 ± 0.1	11	4.3 ± 0.2	7	M
BGI	−0.18 ± 0.00	7.8 ± 1.4	−2.1 ± 0.1	12	4.7 ± 0.2	7	M
BNE[c]	−0.06 ± 0.05	8.1 ± 2.2	−1.3 ± 0.0	2	2.4 ± 0.2	7	M
CAR	−0.01 ± 0.01	7.2 ± 1.3	−1.0 ± 0.1	1	0.3 ± 0.1	6	W
CMA	−0.14 ± 0.02	10.0 ± 2.3	−1.9 ± 0.1	12	1.8 ± 0.1	7	E
DND	−0.12 ± 0.01	10.8 ± 1.7	−1.0 ± 0.0	4	2.4 ± 0.1	7	M
ESP	−0.09 ± 0.00	11.6 ± 1.6	−0.6 ± 0.0	12	0.4 ± 0.1	9	W
ETL	−0.13 ± 0.01	13.8 ± 2.0	−1.1 ± 0.1	1	2.0 ± 0.1	8	N
FWI[c]	−0.22 ± 0.01	8.5 ± 2.1	−2.6 ± 0.0	4	3.1 ± 0.2	7	M
HAA	−0.01 ± 0.01	7.0 ± 0.8	−0.4 ± 0.0	1	0.9 ± 0.0	8	W
HFM	−0.10 ± 0.02	10.7 ± 2.2	−2.3 ± 0.1	11	2.3 ± 0.1	6	E
HIL	−0.15 ± 0.01	10.6 ± 1.6	−1.4 ± 0.1	12	3.4 ± 0.1	7	M
LEF[b]	−0.14 ± 0.01	15.3 ± 2.4	−2.0 ± 0.1	1	4.2 ± 0.2	8	M
NHA	−0.12 ± 0.01	12.8 ± 2.1	−2.2 ± 0.1	11	2.4 ± 0.1	8	E
OIL[c]	−0.19 ± 0.01	5.2 ± 1.5	−2.2 ± 0.1	2	2.3 ± 0.2	8	M
PFA	−0.14 ± 0.01	13.8 ± 1.6	−0.8 ± 0.0	4	1.4 ± 0.1	8	W
RTA	−0.40 ± 0.15	1.1 ± 0.5	0.1 ± 0.0	2	0.5 ± 0.0	6	S
SCA	−0.09 ± 0.03	7.2 ± 1.7	−1.9 ± 0.0	12	1.0 ± 0.1	6	E
SGP	−0.07 ± 0.02	8.0 ± 2.8	−1.5 ± 0.1	12	0.7 ± 0.1	9	M
TGC	−0.02 ± 0.02	6.6 ± 1.1	−0.9 ± 0.1	3	0.5 ± 0.1	6	S
THD	−0.08 ± 0.02	8.8 ± 1.5	−0.8 ± 0.1	11	0.1 ± 0.1	9	W
WBI	−0.12 ± 0.03	10.1 ± 2.6	−1.5 ± 0.1	10	3.4 ± 0.2	7	M

[a]Lag (fraction of years) is the time between the site summer minimum and the summer minimum at MLO site. Amplitude (ppm) is the average amplitude of the seasonal cycle based on a fit of four annual harmonics to the column integrated seasonal cycle. The minimum (winter) gradient is the minimum slope of the vertical gradient (ppm of CO_2/km), and the maximum (summer) gradient is the maximum slope of the vertical gradient (ppm of CO_2/km). Gradients are calculated as the slope of measured mole fractions between 5000 masl and the lowest altitude sampled. Uncertainty (standard deviation) has been calculated using a Monte Carlo simulation where individual observations are varied based on the RMS error of the original fit to data. Regions are (M)id-West, (W)est, (E)ast, (S)outh, and (N)orth. Max and Min define the average month of the year when the seasonal maximum and minimum vertical gradient are observed.
[b]Profiles are below 6000 masl.
[c]Terminated site that was occupied for less than 2 years.

(AAO, BGI, BNE, FWI, HIL, LEF, and SGP) or east (CMA, HFM, NHA, and SCA), the deviations in the free troposphere from the MLO seasonal trend are significantly smaller suggesting a net transport of mid-Pacific free tropospheric air from MLO in a diagonal direction, northeastward, not just eastward, across the continent. At TGC, where samples are taken off the Gulf Coast of the United States, the only deviations from the seasonal trend at MLO are in the boundary layer. The transport mechanism for bringing air from the Gulf Coast into the continental United States will be explored in greater detail with mean air mass transport fields (section 4.3).

Although the climatological monthly mean offset above 4 km from the MLO seasonal trend is never more than ±2 ppm in the lower-latitude, midcontinent, and East Coast sites, there is significant variability (±5 ppm). In particular, the summertime (JAS, Figure 12) vertical mixing tends to flatten out the gradient between the boundary layer and the free troposphere leading to greater offsets from MLO above 4 km. This is important because most of the eastern and southern sites show a significant decoupling between the boundary layer and the free troposphere throughout the rest of the year.

3.2.4. Decoupling Between Boundary Layer and Free Troposphere

As pointed out above, the annual climatology for CO_2, CH_4, CO, N_2O, and SF_6 (Figures 5–9) suggests that air coming onto the continent along the west coast is vertically well-mixed; however, there is a significant gradient between the boundary layer and free troposphere for most sites in the Mid-West and East Coast. There is also a significant phase shift in the seasonal cycle between the boundary layer and the free troposphere at these sites. The magnitude of the lag is demonstrated by comparing the seasonal cycle of the lower 150 mbar at HAA with the samples taken in the lower 150 mbar at all of the other sites (Figure 10). The enhanced vertical gradients between ~500 and 5000 m above ground level (masl) at the Mid-West and East Coast sites are shown with the minimum (winter) or maximum (summer) vertical gradients for each site (Table 3 and Figure 12). These gradients were calculated by using the deseasonalized trend at MLO to detrend each aircraft measurement and bin each measurement by

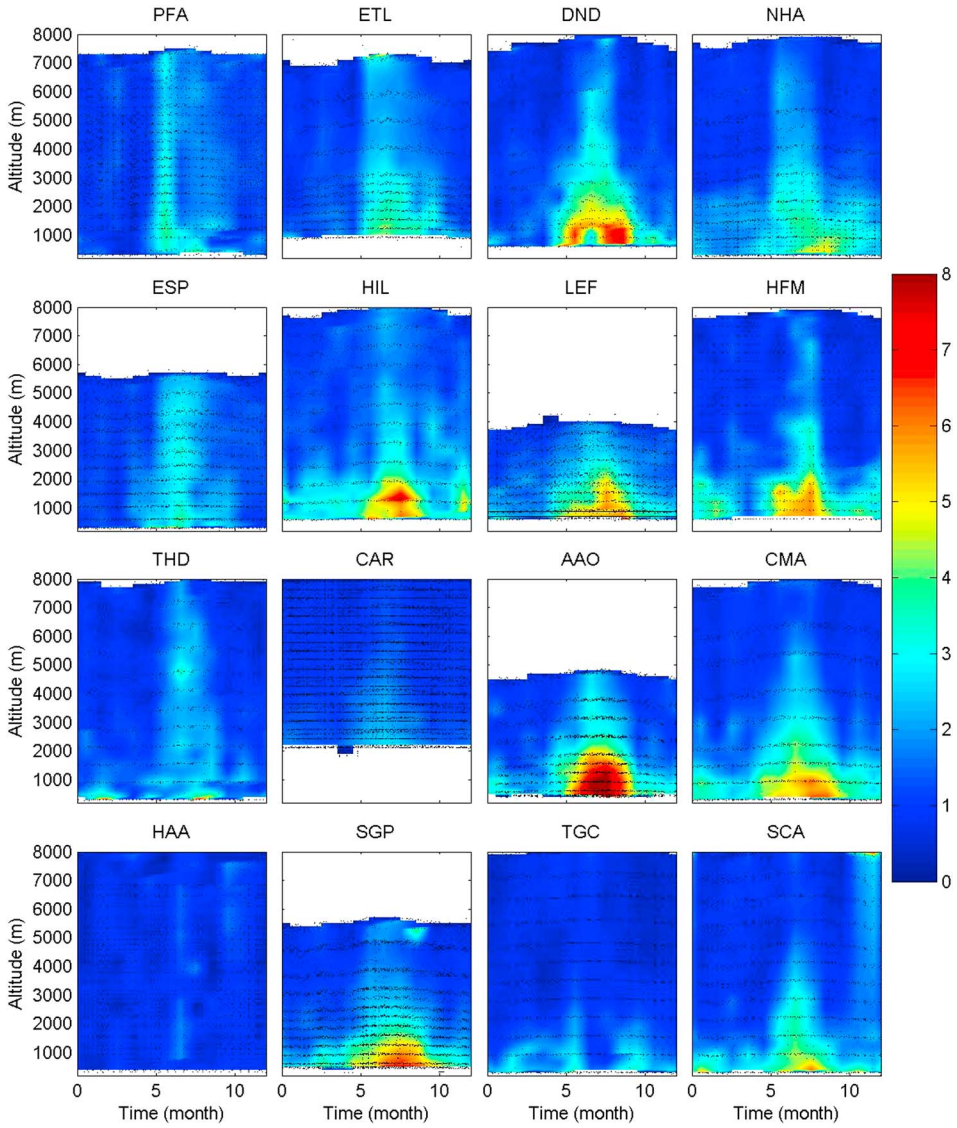

Figure 11. The standard deviation in CO_2 in vertical profiles for each month of the annual the climatology at 16 sites from the NOAA/ESRL Global Greenhouse Gas Reference Network Aircraft Program. Each panel shows the standard deviation in the difference of CO_2 mole fraction (ppm) from the deseasonalized trend at MLO. The black dots illustrate sample location, and the color matrix is a compilation of vertical profiles measurements binned in monthly increments. Vertical discontinuity in the variability in boundary layer is indicative of a recent change in boundary layer sampling protocol at certain sites (e.g., PFA) or simply lack of samples at a certain altitude and time.

month of the year. A least squares fit of a linear polynomial to all the data from 500 magl to 5000 masl for each month of the year was used to determine the vertical gradient for each month.

While the West Coast sites (PFA, ESP, and THD) have relatively small vertical gradients in both winter and summer, many of the midcontinent sites (HIL, BNE, DND, ETL, and LEF) have large vertical gradients during the summer. This is driven by the fact that most of these sites are near agricultural regions responsible for large net ecosystem production (NEP) of organic carbon that results in a large drawdown in atmospheric CO_2 [*Lauvaux et al.*, 2012]. Despite this difference in vertical gradients, there is some similarity in the fact that the West Coast and Mid-West sites both have relatively large offsets in the timing of the seasonal cycle relative to MLO (Table 3). At the midcontinent the difference in timing of the midsummer drawdown in CO_2 is the result of a very rapid drawdown from April to July in the near-surface CO_2 mole fraction relative to MLO. The exception is CAR which is downwind of a large arid region. At the East Coast sites, both the temporal offset from MLO in the seasonal cycle and the vertical gradients decrease relative to

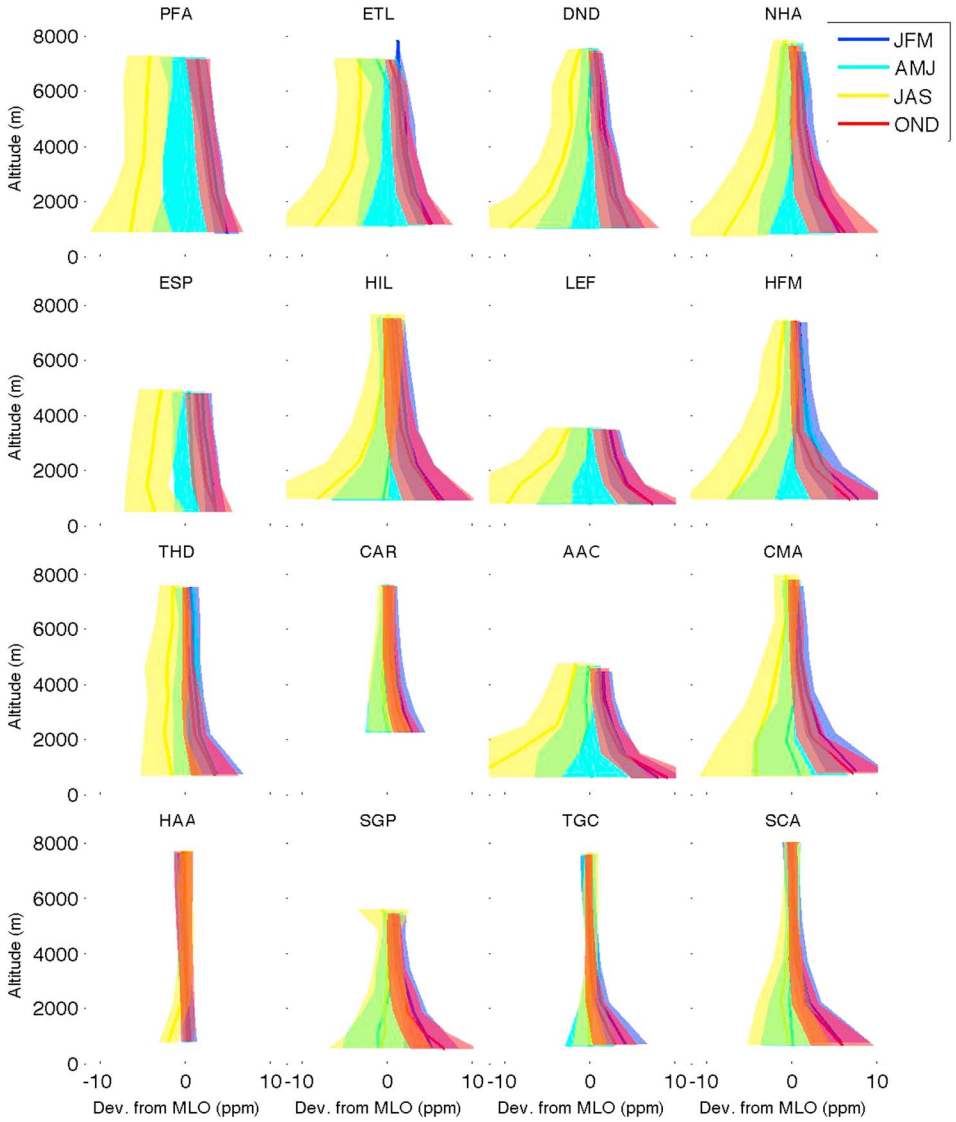

Figure 12. Deviation from seasonal cycle at MLO. Each panel shows offset from CO_2 mole fraction (ppm) from seasonal trend (fit of four annual harmonics) at MLO. Dark blue line and shading show mean and standard deviation, respectively, in January, February, and March (JFM). Light blue line and shading show mean and standard deviation, respectively, in April, May, and June (AMJ). Yellow and light yellow shading show mean and standard deviation, respectively, in July, August, and September (JAS). Red and light red shading show mean and standard deviation, respectively, in October, November, and December (OND). Averaged lines are based on binned averages within a 3 month period and six to eight altitude bins, which have been adjusted to capture significant vertical gradients at each station.

those observed in the Mid-West. As air masses move from the Mid-West to the East Coast, the phase shift in the seasonal cycle shrinks from ~1.7 months to ~1.2 months (Table 3). The vertical gradients in summer and winter also get smaller, presumably due to vertical mixing as the air masses travel east and because of the addition of fossil fuel CO_2. The latter contributes to a more negative gradient in the winter. Mid-West sites in the heart of the agricultural region like BGI, HIL, LEF, and WBI have respective summertime vertical gradients of 4.7 ± 0.2, 3.4 ± 0.1, 4.2 ± 0.2, and 3.4 ± 0.2 ppm km^{-1} but relatively weak wintertime gradients of -2.1 ± 0.1, -1.4 ± 0.1, -2.0 ± 0.1, and -1.5 ± 0.1 ppm km^{-1} (Table 3). By contrast, Northeast Coast sites like NHA and HFM have summertime vertical gradients of 2.4 ± 0.1 and 2.3 ± 0.1 ppm km^{-1} and wintertime vertical gradients of -2.2 ± 0.1 and -2.3 ± 0.1 ppm km^{-1}, respectively. In many cases the vertical gradients that we observe are predominantly a function of the magnitude of the uptake or emissions, though transport also plays a role (see section 4.3). In the midcontinent the summertime drawdown period at

these sites is both short and intense compared to the wintertime emissions; this results in larger vertical gradients in the summer. At the East Coast sites the combination of ecosystem respiration and fossil fuel emissions help drive a more intense CO_2 emissions flux, which leads to smaller (more negative) vertical gradients in the winter compared to the Mid-West sites.

3.3. Transport

Examining the seasonal variability of the winds near each of the sites (Figure 13) and the predicted surface influence from air-mass back-trajectory calculations (Figures 14 and 15) aids in understanding the drivers of spatial and temporal variability in site CO_2 climatologies.

As a trace gas, CO_2 is unusual because its sinks and sources are mostly confined to the land or ocean surface with the exception of some emissions from aircraft. From this perspective an understanding of where an air parcel measured by an aircraft profile last was in the planetary boundary layer is extremely helpful in understanding what controls the variability in CO_2 of the air masses measured. To get a picture of the surface influence for each site, the Hybrid Single Particle Lagrangian Integrated Trajectory Model (HYSPLIT Model, http://ready.arl.noaa.gov/HYSPLIT.php) [*Draxler and Rolph*, 2012] was used in conjunction with the EDAS reanalysis meteorological fields to track air masses starting at 500, 1000, 2000, and 4000 magl from each site backwards in time over a 6 day period starting at the actual time of each sampling flight from 2006 through 2009. The average fraction of the particles released at each site from each back-trajectory below 200 m above ground level (magl) was then averaged in each model grid cell for each month of the year in order to get a monthly average surface influence for each site. By binning the average fraction of particles below 200 magl into monthly bins, biases produced in a given month or site due to differences in sampling frequency from month to month are diminished.

To provide a slightly different perspective, a climatology of winds for each site (Figure 13) is also examined. The average monthly NCEP horizontal winds were compared to the surface influence analysis (http://www.cpc.ncep.noaa.gov/products/wesley/reanalysis.html, Figure 14). As expected, the compilation of the surface influence provided by all the sites throughout the year (Figure 14) suggests that the surface influence based on actual backward particle release experiments is not very different from what might be expected from the average climatology of horizontal mass transport, which provide very little information about the role of vertical mixing. The exception to this is the influence of boundary layer air off of the East Coast of the continental US, which does not show up as clearly from the average monthly NCEP horizontal wind climatologies. On close inspection there is also a "shadow zone" east of the Sierra and Rocky Mountain ranges where there is very little influence from surface processes that could be an artifact of the EDAS reanalysis, which has a nominal resolution of 40 km.

A breakdown by individual sites provides a better spatial picture of the surface influence of the different sites (Figure 15). Starting with PFA in the northwest, the footprints suggest that much of the surface influence comes directly from the south in the North Pacific Ocean. Similarly, both ESP and THD show significant surface influence from the North Pacific Ocean. It is also clear from the THD footprints that measurements are significantly affected by local land sources. The large enhancements in the boundary layer CO at this site demonstrate this local influence as well (Figure 6).

The surface influence of the Colorado site (CAR, not shown in Figure 15) illustrates how important this site is for detecting changes in the southwestern region of the US. For the Midwest sites (represented by LEF in Figure 15), the surface influence is centered in the midcontinent region. The surface influence from DND (and ETL, not shown in Figure 15) shows more influence from the North Pacific than the other midcontinent sites, which might explain the anomalies in the CO_2 seasonal cycle in the higher-altitude samples at these sites. In contrast, the southern site TGC shows significant influence from the Texas Gulf Coast. Moving to the southeast coast, SCA shows significant influence from the east, as well as areas to the west in the southeastern corner of the US. Moving north, samples taken at CMA are likely to be influenced by surface processes in the Mid-Atlantic, as well as the rest of the continental US to the west. This is also true of HFM and NHA.

Looking at the wind direction and speed from 1000 to 350 mbar (Figure 13) it is clear that the annual climatological picture is affected by seasonal changes in wind speed and direction. In particular, winds at PFA change from a southwest direction in the winter to south in the summer with significant decreases in

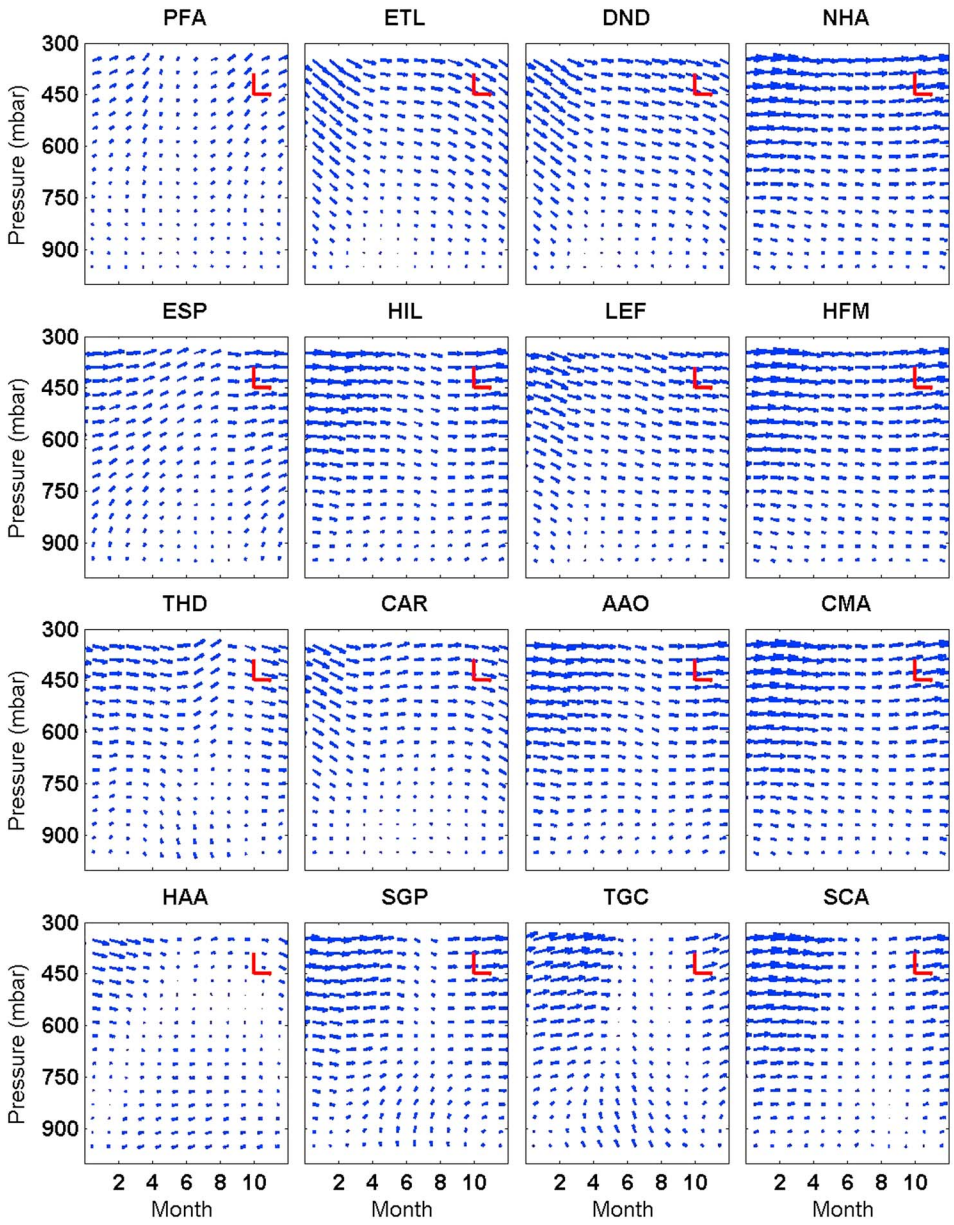

Figure 13. Interpolated monthly average horizontal winds at 16 sites from the NOAA/ESRL Aircraft Network. Each panel shows the mean wind vector along pressure surfaces for each month of the year using NCEP/NCAR Reanalysis I [*Kalnay et al.*, 1996]. Red vectors indicate vector scale (m s^{-1}).

wind speed. In contrast, Midwestern sites like ETL, DND, LEF, and even CAR have winds coming from the northwest in the winter and directly from the west in the summer at the higher altitudes consistent with seasonal changes in the jet stream. Lower-altitude wind directions at each site suggest that these same Midwestern sites are more influenced by the regions to the southwest during the summer and the northwest during the winter. Southern sites like SGP and TGC are notable for the significant enhancement of winds from the south during the summer.

3.4. Horizontal Flux of CO_2 Over North America

Combining the mass transport (Figure 13) with the deviations in CO_2 mole fraction from the deseasonalized trend at MLO over a single climatological year (Figure 5), it is possible to estimate the net horizontal mass transport of CO_2 at each site on a monthly basis at multiple altitudes (Figure 16). *Crevoisier et al.* [2010] used this same approach to estimate the net release of CO_2 from the continent by first interpolating the

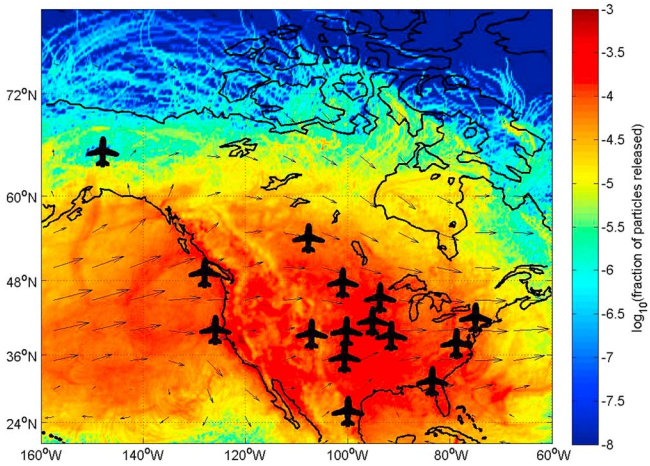

Figure 14. Footprint for samples taken from 2004 to 2010 in NOAA/ESRL Global Greenhouse Gas Reference Network Aircraft Program. Fraction of particles released that stay below 200 magl. This experiment released 100 particles from each site location at altitudes of 500 m, 1000 m, 2000 m, and 4000 m on days corresponding to sampling times.

deviations from the deseasonalized trend at MLO over the whole continent and convolving and summing that with a monthly climatology of mass transport.

This analysis examines key features of the net horizontal mass transport of CO_2 on a monthly basis from ground to 8000 masl (Figure 16) at each site in North America to better understanding how the direction and magnitude of the mean wind patterns act on the deviations from trends at MLO noted in the climatological profiles of CO_2 mole fractions (Figure 5) to produce a "net" horizontal mass flux of CO_2. This is different from the total horizontal mass flux of CO_2 because it is a product of the transport multiplied with the deviation from the deseasonal trend at MLO.

3.4.1. Spatial and Temporal Variability of Winds

In considering the spatial and temporal variability of the net horizontal mass flux of CO_2 over North America it is important to note two factors in mass transport that will change the net flux: (1) a consistent increase in wind speed with altitude and (2) a decrease in wind speed and change in direction during July and August.

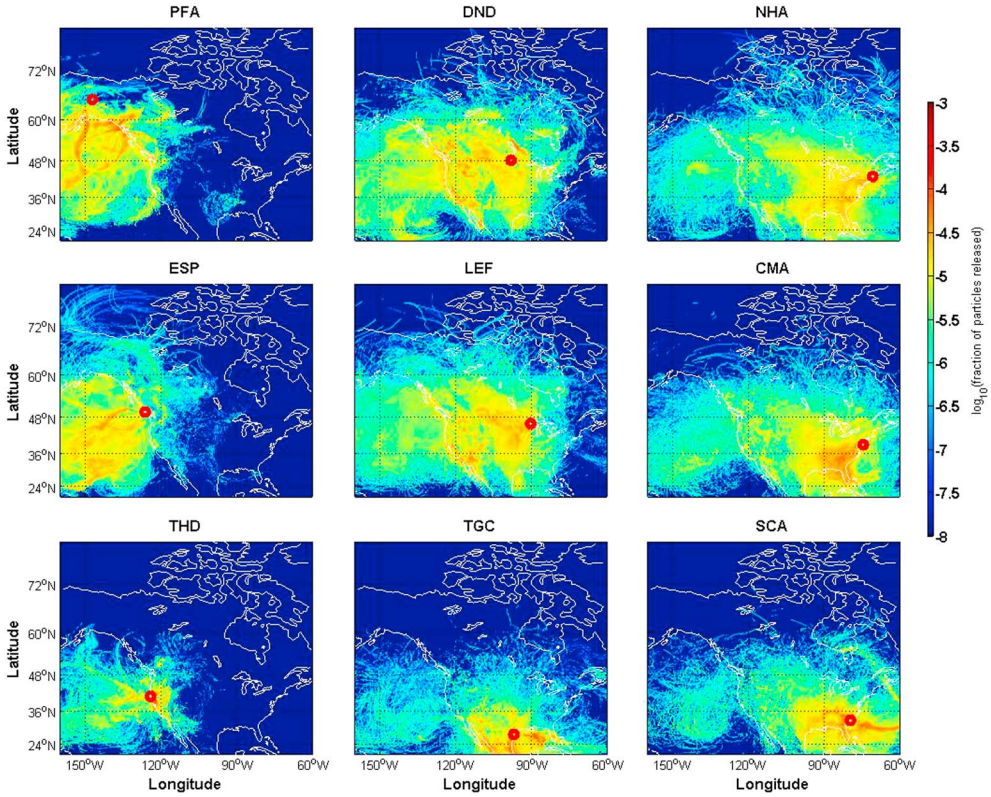

Figure 15. Site footprints for NOAA/ESRL Global Greenhouse Gas Reference Network Aircraft Program. Fraction of particles that stay below 200 magl using HYPSLIT. This experiment released 100 particles from each site location at altitudes of 500 m, 1000 m, 2000 m, and 4000 m on days corresponding to sampling times from the year 2004 to 2010.

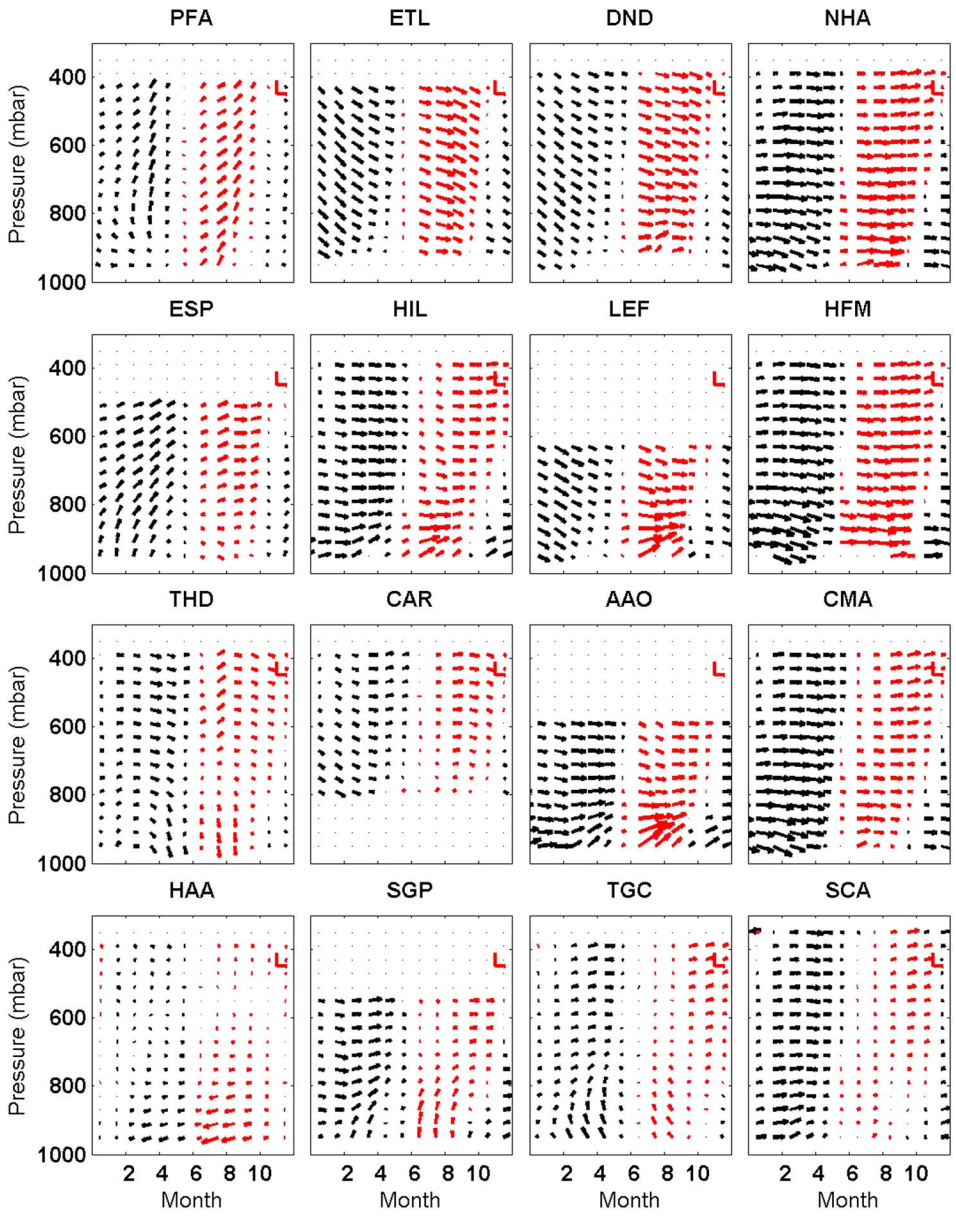

Figure 16. Net monthly anomaly mass flow of CO_2 (mol CO_2 m^{-2} s^{-1}) as a function of altitude at NOAA/ESRL sites with reference to deseasonalized trend at MLO. Red vectors indicate vector scale (10^{-3} mol CO_2 m^{-2} s^{-1}). (red) negative anomaly (relative to MLO) flow and (black) positive anomaly flow.

3.4.1.1. High-Altitude Mass Transport

With the large increase in wind speeds with altitude at all sites (Figure 13), it is expected that the net horizontal mass transport of CO_2 would also increase with altitude. While it is true that small deviations from the deseasonalized trend at MLO at higher altitudes are amplified by higher transport winds, these deviations are not consistent throughout the year. Enhancements in net horizontal mass flux of CO_2 are most obvious in the "shoulder" seasons (March, April, May; August, September, and October) where the MLO seasonal cycle is out of phase with most of the aircraft sites and therefore have higher difference from deseasonal trend at MLO. In the Northwest the high-altitude net mass flux is driven by large enhancements in the spring and rapid depletions in the summer relative to MLO. These CO_2 deviations are largest in Alaska (PFA), where the net mass flux is relatively small because the wind speeds at this site are low relative to the other sites in the network. Moving eastward across the continent, the high-altitude

winds amplify more subtle deviations in CO_2 mole fraction above 4000 masl due to vertical mixing of CO_2 anomalies coming from the boundary layer.

3.4.1.2. Summertime Mass Transport

Changes in summertime winds highlight three important features in the monthly net horizontal mass flux patterns. The first is the marked change in wind direction in the summer time. In general all the sites show a southerly shift in wind direction. In the northwest, high-altitude winds shift from westerly to southwesterly, and winds in the northern Mid-West and northeast sites shift from northwesterly to westerly from winter to summer. In many of the northwest sites (THD, ESP, PFA, ETL, and DND), the climatological wind shifts are more pronounced at lower altitudes. At PFA a shift can be seen southeast to the south below 750 mbar and at DND winds go from the northwest to the southwest between winter and summer. The second feature is a decrease in wind speeds at all sites during the summer. This decrease in wind speed acts to amplify measured drawdown of CO_2 mole fractions in the boundary layer at both midcontinent and East Coast sites because the air masses spend more time over these areas than they would at other times in the year. It should be noted that the decrease in summertime horizontal wind speeds counters the rectifier effect as originally defined [*Denning et al.*, 1999] where increases in boundary layer height act to dilute the effect of summertime uptake on measured mole fractions. Despite these decreases in wind speeds, the net horizontal mass flux of CO_2 anomalies in the summertime boundary layer still dominate the net mass flux seen throughout the column at the midcontinent and East Coast sites because of the large decrease in CO_2 mole fraction relative to MLO.

Summertime winds in the Gulf Coast at TGC and to a lesser degree at SGP are also significantly different from those of other seasons. The boundary layer winds are almost 135° different from the free troposphere flow in most seasons. Here the free troposphere winds significantly decrease, while the boundary layer mean winds significantly increase in the summer. The resulting incoming air closely resembles air measured at MLO (Figure 12). The net result is a source of "MLO like" clean air coming into the continent which, below ~4000 masl, is slightly enriched in CO_2 relative to productive inland regions. The suggestion of clean air is confirmed by the CO profiles at TGC, which show very little difference from what would be predicted from deseasonalized trends at MLO during the summer (Figure 6).

3.4.2. Net Annual CO_2 Flux

The net mass flux of CO_2 for winter/spring (November through May) and summer/fall (June through October) are summed to determine the net annual mass flux over each site for a single climatological year (Figure 17). Despite the lower wind speeds below 4000 masl, boundary layer processes make an important contribution to the net flux of CO_2 over the continent. In particular, the short summertime but intense drawdown of CO_2 during June, July, and August creates a large signal at midcontinent sites such as AAO, HIL, and LEF and at east coast sites such as NHA, HFM, and CMA. East Coast sites also show strong wintertime net horizontal mass fluxes at low altitudes resulting from the combined effect of fossil fuel and net respiration of the biosphere [*Miller et al.*, 2012].

In map view (Figure 18) the summertime and wintertime horizontal flux densities (MgC m^{-1} $mbar^{-1}$) have been plotted at each site as well as the annual column-average wind speed (up to 8000 masl). The column-average wind speeds emphasize the west-to-east flow of the high-altitude wind vectors rather than the more subtle northerly and southerly components of the boundary layer wind vectors. As expected, the net seasonal horizontal fluxes of CO_2 closely follow the column-average wind speed. This picture also corroborates the idea that as air masses pass from the West Coast to the East Coast there is significant accumulation of both biological and fossil fuel inputs.

Crevoisier et al. [2010] uses the same NOAA/ESRL Global Greenhouse Gas Reference Network Aircraft Program data set corrected for the deseasonalized trend at MLO used in this study to calculate the net continental flux by interpolating the site data over a major portion of the continental area and calculating the horizontal fluxes at the edge of regional boundaries. The net change within each region can be interpreted as the regional flux. *Crevoisier et al.* [2010] took one more step by subtracting the known fossil fuel production in a region to estimate the total biological uptake. The net result showed that using data from 2004 to 2006 the total annual flux was 1.22 ± 0.41 PgC yr^{-1}. With an estimated 1.73 ± 0.04 PgC yr^{-1} of fossil fuel emissions over that period, the net biological uptake was estimated to be 0.5 ± 0.4 PgC yr^{-1}. Breaking the continental US into regions, it was shown that 52% of the uptake was in the Mid-West states, a result that can also be inferred from the net seasonal horizontal flux densities at each site (Figure 18).

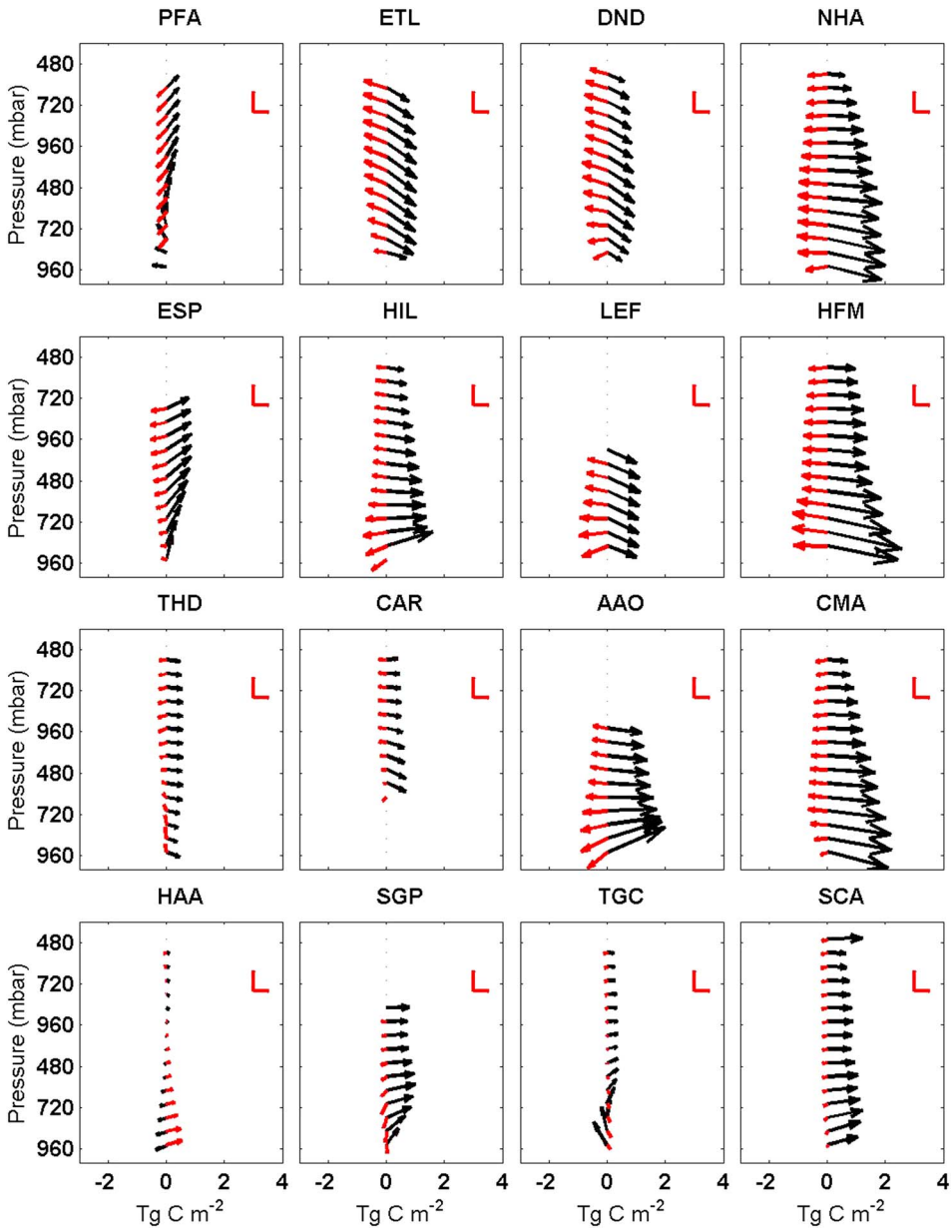

Figure 17. Mass flow anomaly for winter (black, November to May) and summer (red, June to October). Net monthly mass flow of CO_2 (MgC m^{-2}) as a function of altitude at NOAA/ESRL sites with reference to deseasonalized trend at MLO. Red vectors indicate vector scale (0.5 MgC m^{-2}).

4. Discussion

Although there are many features of the NOAA/ESRL Global Greenhouse Gas Reference Network Aircraft Program data set that could be discussed in further detail, two points are most critical. The first point focuses on the temporal sampling requirements of the NOAA/ESRL Global Greenhouse Gas Reference Network Aircraft Program, and the second point focuses on the drivers of the strong seasonal cycle that is observed at PFA and other sites in the Northwest region of North America.

4.1. Sampling Biases and Aliases

The *Crevoisier et al.* [2010] study demonstrates the usefulness of the NOAA/ESRL Global Greenhouse Gas Reference Network Aircraft Program data in estimating the time-averaged regional fluxes. Because the

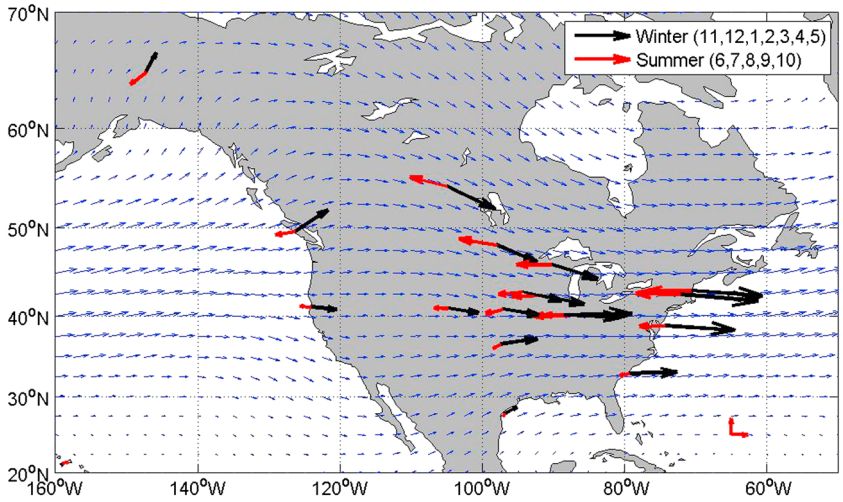

Figure 18. Net seasonal CO_2 anomaly mass flux (MgC m^{-1} $mbar^{-1}$ a^{-1}) calculated from top to bottom of sampled altitude range (Table 2) at each site in the NOAA/ESRL Global Greenhouse Gas Reference Network Aircraft Program. Winter mass flux (black) is calculated from November through May with positive offsets from MLO shown as east and north vectors. Summer (negative) anomaly mass flux (red) is calculated from June through October. Lower left vector shows 4 MgC m^{-1} $mbar^{-1}$ calculated in east and north directions. Average annual winds (300–1013 mbar) are shown in blue.

calculation of the horizontal flux to 8000 masl does not require any assumptions of vertical mixing beyond the linear interpolation used to infer gradients between the 12-flask sample altitudes in each profile, it avoids a major pitfall of inversions based on surface data, which rely on estimates of vertical transport [e.g., *Stephens et al.*, 2007]. However, it is important to recognize that *Crevoisier et al.* [2010] estimated mean regional fluxes over North America based on climatologies presented in this study. From that study two questions arise: (1) What sampling frequency is required to capture interannual variability? (2) What sampling biases arise from the current sampling program, which sample mostly on clear days in the middle of the day?

4.1.1. Capturing Interannual Variability

To answer the first question, it is helpful to think about how one might detect interannual variability in the integrated column measured by aircraft. The integrated column of CO_2 from 0 magl to 8000 masl captures the changes in the boundary layer as well as changes that we have shown exist at higher altitudes (Figure 17). The integrated signal also, as it turns out from the analysis described below, requires far less sampling to recover the same fraction of variability. In other words, despite the decrease in signal (e.g., the amplitude of the seasonal signal or the synoptic variability) observed in the column-integrated CO_2, the correlation timescale is much longer than what is observed in the boundary layer. With a longer correlation timescale, there is also a decrease in required sampling frequency needed to capture critical features and gradients in CO_2 mole fraction time series at an individual site. This can be shown by subsampling CarbonTracker at individual sites and measuring either the decrease in variability or increase in root mean square (RMS) of the residuals relative to the high-resolution time series (1.5 h). This analysis suggests that more than 80% of the variability in the column-integrated mole fraction of CO_2 is captured with sampling intervals as long as 45 days and that the seasonal cycle accounts for more than 90% of that variability observed at any site. However, reproduction of variability in a time series does not help to quantify how much sampling will be needed to detect interannual variability. One approach is to smooth the residuals of equation (1) with a 1.5 month FWHM smoother [*Thoning et al.*, 1989] from each subsampling of CarbonTracker and compare that with a smoothed fit of the original high-resolution time series at each site (Figure 19). A 1.5 month smoother has been used because a persistent deviation over that period is likely to be caused by interannual variability in the CO_2 seasonal cycle. Deviations over this time frame might help detect a change in seasonal amplitude caused by a drought, early spring, a wet summer, or a sudden change in anthropogenic emissions. It should be noted that the results of this analysis do not change significantly if the smoothing time period is doubled or halved.

In the case of anthropogenic emissions, the change in the average column CO_2 mole fraction of an air mass traveling across the country is 0.8 ppm assuming that it takes 5 days to travel across the contiguous lower 48 states of the U.S. (~8.4×10^{12} m^2) and that an aircraft profile is measuring the change in signal up to 8000 masl (two thirds of the atmospheric column which is 3.55×10^5 mol of air m^{-2}). Thus, to see a change in the average column CO_2 mole fraction at a single site, it might be necessary to reduce the uncertainty in the smoothed residual of equation (1) to less than 0.2 ppm (25% of the average fossil fuel CO_2 enhancement that we expect as an air mass travels across the continent).

There are a few insights to be gained from this analysis. First, there is a significant increase in uncertainty (RMS of deviations from the original high-resolution time series) with an increase in sampling intervals from 1 to 12 days. This increase in uncertainty significantly levels off from 12 to 50 day sampling intervals. These two observations are consistent with the synoptic scale of fronts (10–12 days) moving across the country and the predominance of the seasonal cycle in the variability observed for the column average CO_2 from 0 to 8000 masl, respectively. This analysis suggests that the increase in uncertainty as sampling intervals are increased is larger at sites in the eastern and northern part of the continent. This is consistent with an increase in spatial CO_2 gradients caused by the accumulation of both biogenic and anthropogenic fluxes as the air masses move across the continent. Although background sites that capture air coming predominantly from the Pacific Ocean (HAA, ESP, PFA, and THD) only need to be sampled at 3–16 day intervals to capture deviations of 0.2 ppm, East Coast and midcontinent sites need to be sampled daily to capture subtle changes in the 2 month smoothed fit of the data.

One can also break down the RMS of residuals by month at different sampling intervals (Figure 20). Aircraft observations show significantly more variability during the summer months, and sampling intervals at each site need to be decreased during the summer months in order to capture this variability. This is illustrated by a twofold increase in RMS to the residuals in July and August compared to other months.

There are a few caveats to this analysis that need to be stressed and further examined in future studies. This approach considers each aircraft profile independently of other ground, tower, or aircraft sites that provide valuable constraints given the similarity between sites like NHA and HFM that we observe for CO_2 mole fractions. To properly evaluate how other ground, tower and aircraft sites help to reduce the sampling interval required to detect interannual variability a full-scale observing system simulation experiment (OSSE) would need to be designed to account for the covariance of CO_2 mole fractions and differences in sampling frequency of ground, tower, and aircraft sites. As mentioned above, it would also be useful to define the variability that we are trying to measure in terms of events such as drought or an increase in anthropogenic emissions rather than an arbitrary time period; however, this analysis does provide a conservative estimate of the sampling required to observe persistent changes over a 1.5 month period, which generally lead to interannual variability in the seasonal cycle of CO_2. Comparisons with high-resolution ground sites suggest that CarbonTracker does capture synoptic variability; however, it is unclear how much subgrid scale variability may contribute to this sampling experiment.

4.1.2. Time of Day and Weather Biases

There are several other studies that have tried to understand the biases that might exist from the time of sampling. *Stephens et al.* [2007] suggest that at local noon, when most aircraft profiles are made, a vertical profile is generally very representative of the average daily column mean, suggesting that profiles collected at local noon will not be biased compared to multiple samples taken throughout the day; however, there is no doubt that because there is a diurnal cycle in the integrated column of CO_2 mole fraction, significant deviation from noontime sampling will manifest itself as a bias for one site relative to another if sampling time is not taken into account. This effect is likely to be most pronounced at sites with a strong local biological signal during the summer months where the CO_2 mole fraction decreases by several μmol/mol over the day in the boundary layer. In this instance a site sampled at 10:00 local time will have a weaker summer time minimum than the site sampled at 14:00 local time and, more importantly, the vertical gradients will be more pronounced.

Another potential bias arises from the fact that although pilots are encouraged to fly in a variety of conditions, flights are more likely to happen on clear-weather days. Large biases due to differences in surface to free troposphere [*Stephens et al.*, 2007] and mean column [*Corbin et al.*, 2009; *Crevoisier et al.*, 2010] CO_2 mole fractions have been noted due to clear-weather sampling biases. In particular, these biases seem to be

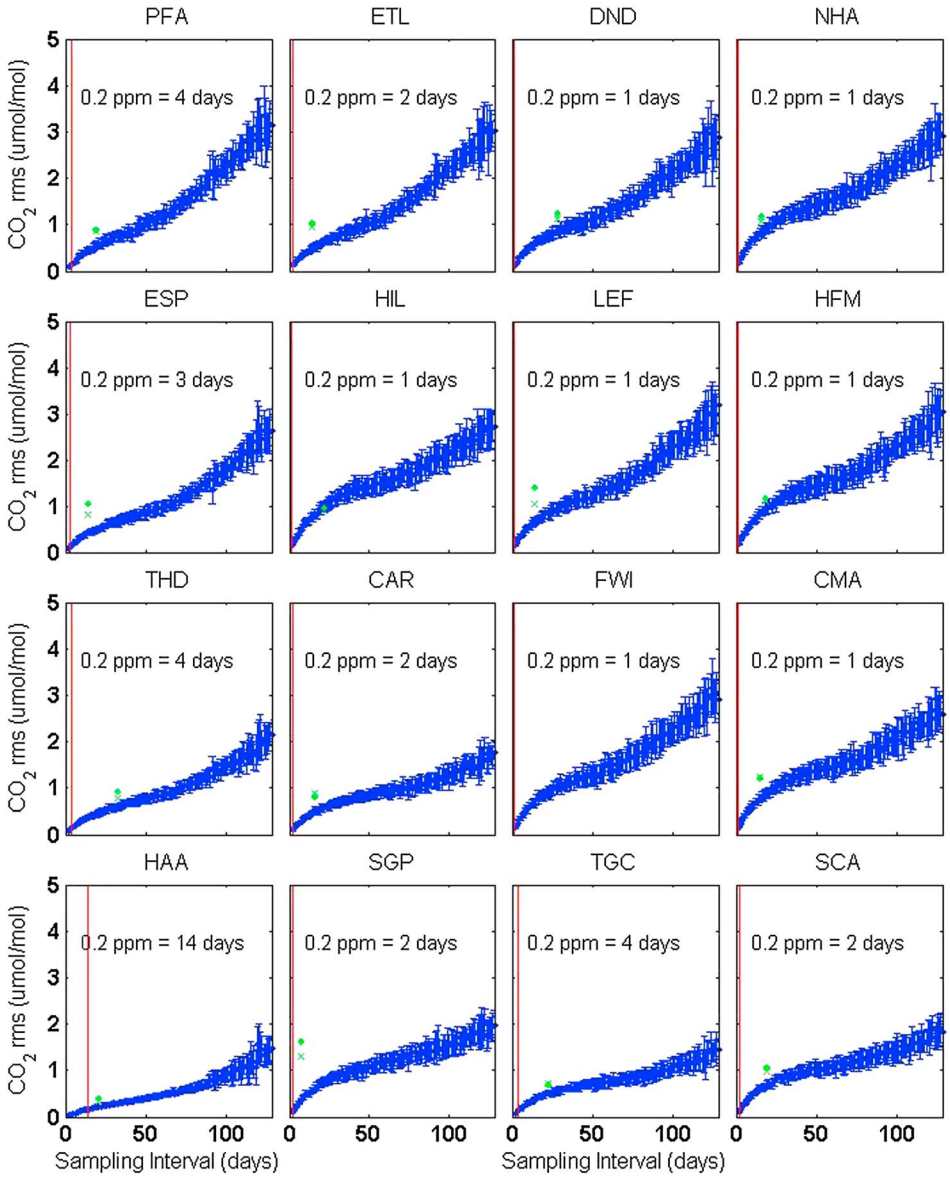

Figure 19. RMS deviation in 1.5 month smoothed fit with change in sampling interval—The average CO_2 mole fraction of the levels 1–12 in Carbontracker (http://www.esrl.noaa.gov/gmd/ccgg/carbontracker/) are sampled at each site at different average time intervals over 7 year (2006–2012) time period. Blue points are the mean of the root mean square (RMS, μmol/mol) deviation between the sampling trial and the original daily sample. Error bars show standard deviation of 30 different sampling trials at each sampling interval. The sampling trials are created by varying the hour and day that sampling is started, as well as the interval between each sample. Thus, each sampling trial has the same average sampling interval but slightly different sampling intervals between successive sampling times over the course of a sampling trial. Sampling intervals can vary by as much as 50% of the mean sampling interval over the 7 year time series. The residuals of equation (1) are smoothed with 2 month smoother [*Thoning et al.,* 1989], and the RMS deviation of each sampling trial is determined by interpolating the sparse set of observations to daily observations made between the hours of 11 and 2 P.M. local time. The red line is the sampling interval when RMS deviation is >0.2 μmol/mol and is equal to 1 day if the RMS difference at 2 days is greater than 0.2 μmol/mol. For reference, the green dot and cross sign show the RMS deviation between a 1.5 month smoothed fit of equation (1) of actual data and model, respectively, at the average sampling resolution of each site.

most pronounced during the summer, when CO_2 column averages in models predict large differences in carbon photosynthetic uptake during clear sky days versus cloudy days, where lack of light might inhibit photosynthesis and a frontal passage may erase a boundary layer decrease in CO_2. However, it is unclear how accurately these processes have been modeled to correctly reproduce frontal passages and

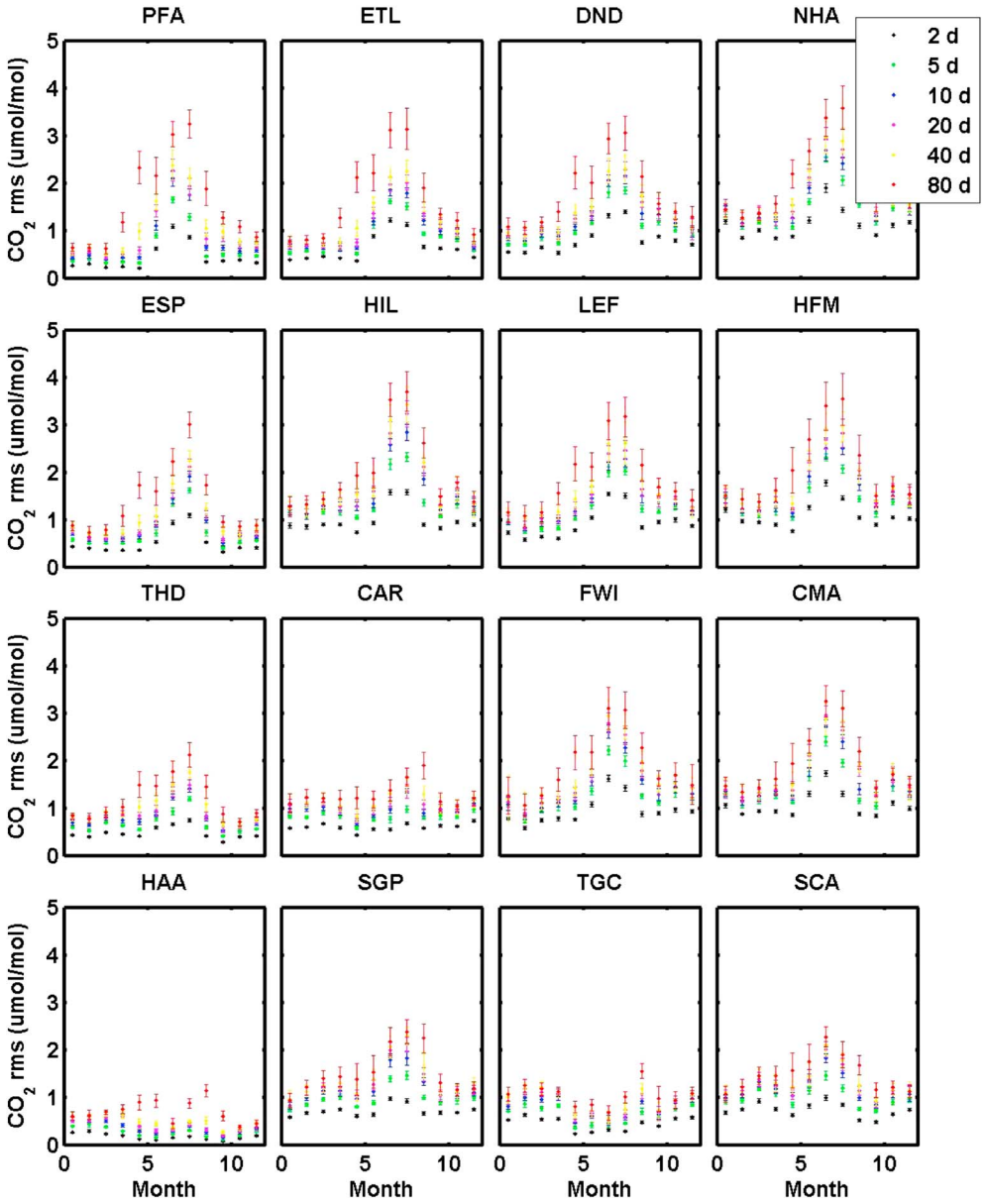

Figure 20. Variation in residual as a result of changing sampling interval by month. The average CO_2 mole fraction of the levels 1–12 in Carbontracker (http://www.esrl.noaa.gov/gmd/ccgg/carbontracker/) are sampled at each site at different average time intervals over 7 year (2006–2012) time period and the residual mean square (RMS) deviation of each sampling trial is determined by interpolating the sparse set of observations onto the original 1.5 h model grid and binning by month of the year. Black, green, blue, magenta, yellow, and red represent average sampling intervals of 2, 5, 10, 20, 40, and 80 days, respectively. As in Figure 19, 30 sampling trials with the same average sampling intervals were used to find the RMS at each point.

photosynthesis. *Law et al.* [2002] note that summertime carbon uptake tends to be greater at many direct flux measurement towers during diffuse rather than under direct sunlight conditions. It is unclear how well these observations have been mimicked in the models, which suggest a small clear weather bias resulting from aircraft sampling.

Yet another possible bias from these aircraft measurements that has not been accounted for in this analysis comes from anomalous transport back-trajectories at a given site. In our analysis we have taken a very simplistic approach to illustrate mean flows of carbon and to infer broad trends in the flow of CO_2 across the continental US. While large outliers that are caused by either local point sources or measurement errors have been eliminated, there are more subtle differences from year to year or in the sampling

conditions that may influence the mean CO_2 in any given month. In boundary layer samples from sites like THD and SGP, there are known transport regimes that lead to enhancements from local sources that represent significant deviation from the mean [*Biraud et al.*, 2013; *Parrish et al.*, 2010]. In the free troposphere, other studies have noted significant changes in the mean column mole fraction of CO_2 at sites like LEF [*Keppel-Aleks et al.*, 2011, 2012], which is particularly sensitive to the location of the jet stream during winter and summer when the latitudinal gradients are likely to highest over that site. The smaller the sampling interval, the less likely it will be that the mean climatologies will be biased by these anomalies.

4.1.3. Summary of Sampling Analysis

In summary, at the average sampling resolution of the aircraft network (~22 days), a significant fraction of the variability (>80%) is sampled at almost all of the sites; however, this sampling frequency is not sufficient to capture the variability that arises from interannual changes in emissions or uptake. Analysis of CarbonTracker suggests that significant improvements in our ability to resolve subtle changes from year to year will come from sampling at intervals less than 12 days. Other studies also suggest that there is the potential for a clear sky bias, which may exaggerate the impact of the summertime draw down. It is unclear whether this fair-weather bias could lead to a transport bias driven by weather dependent biases in transport. Given the expense of flying small aircraft, and the need for a higher sampling frequency and independence of weather conditions, it is clear that profiles made using commercial aircraft could increase sampling frequencies by 100 times assuming 10 instrumented planes were making four profiles a day. This would add significant value to the data set that the NOAA/ESRL Global Greenhouse Gas Reference Network Aircraft Program has provided.

4.2. The Origin of the Strong Seasonal Cycle at PFA

The NOAA/ESRL Global Greenhouse Gas Reference Network Aircraft Program data set offers a unique picture of the distribution of CO_2 in four dimensions—time, latitude, longitude, and altitude. While ground sites have given us a clear picture of CO_2 spatial and temporal gradients that we most often associate with regional and local fluxes, the higher-altitude aircraft measurements suggest that the seasonal cycle of the CO_2 column is largely controlled by large-scale horizontal mass transport and to a lesser extent local fluxes. This is particularly apparent at PFA, where we see a relatively small seasonal cycle in the boundary layer but the amplitude of the integrated-column seasonal cycle is equivalent to or larger than the amplitude at northeast North American sites like NHA or Mid-West sites like HIL (Table 3 and Figure 5), which show large seasonal cycles at the surface. In trying to understand why the integrated CO_2 column at PFA has such a large seasonal cycle, it is useful to consider three points that have been covered in the analysis of the NOAA/ESRL Global Greenhouse Gas Reference Network Aircraft Program data set.

First, the wind directions (and footprints) at PFA (Figures 13 and 15) are predominately from the southwest suggesting that the observed seasonal cycle is the result of transport from lower latitudes. Second, the similarly large seasonal amplitudes in the CO, N_2O, CH_4, and SF_6 profiles and lack of stratification (Figures 6–9) suggest that the enhancement in the seasonal cycle of CO_2 is driven by remote upwind terrestrial processes equivalent to those observed in the eastern part of North America where there are large natural and anthropogenic fluxes acting together to shape the overall seasonal cycle. The third point relates to the timing of the seasonal cycle at PFA; even above 7000 masl measurements at PFA are very depleted relative to measurements at MLO in June and July (Figure 21) much like the boundary layer measurements found at Midwestern sites like LEF and HIL (Figure 5). It should also be noted that eddy covariance studies measuring net ecosystem production (NEP) suggest that despite the high solar irradiance in the early summer, peak NEP is rarely observed before the end of June [e.g., *Ueyama et al.*, 2013] throughout most of Alaska. If the local NEP were driving decrease in the CO_2 observed throughout the atmospheric column, we would expect the NEP to peak much sooner coinciding with the rapid decrease of CO_2 that starts in the beginning of June not the end of June. The fact that both THD and ESP share similar deviation from MLO in early June is further evidence that the anomalies seen at PFA are not likely to be a local effect and more likely to be derived from a lower latitude process where uptake is happening much earlier in the growing season.

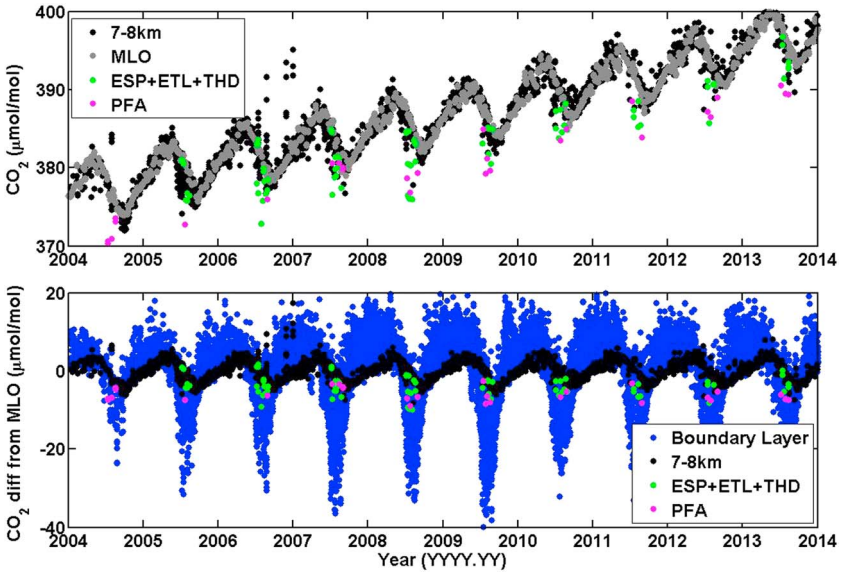

Figure 21. High-altitude CO_2 samples relative to MLO. (top) Time series of CO_2 mole fraction between 7 and 8 km at all NOAA/ESRL Global Greenhouse Gas Reference Network Aircraft Program sites (black) and MLO (gray). (bottom) Same time series detrended using deseasonalized trend at MLO. Blue is all measurements from the NOAA/ESRL aircraft network between 1 and 2 km, and black is all measurements between 7 and 8 km. Magenta and green dots (high-altitude samples between 7 and 8 km) suggest that offsets in the early summer at THD, PFA, and ESP, ETL are synchronous in timing to the offsets seen between 1 and 2 km at most sites through the NOAA/ESRL Aircraft Network.

4.2.1. The Origin of Air Masses Coming to PFA

Expanding on the first and second points, it is likely that the trajectory that contributes the most to observations at PFA is also one that facilitates extensive vertical mixing. The footprint and mean wind patterns (Figures 13 and 15) suggest that all altitudes in the PFA profile are sensitive to air originating from the North Pacific just southwest of PFA in the region where the meander of the Jet Stream is likely to heavily influence the vertical structure of the atmospheric column. This has been demonstrated by the HIAPER Pole-to-Pole Observatory (HIPPO) flights, which showed vertically well-mixed springtime enhancements of CO_2, SF_6, and CO between 45 N and 60 N along a 180 E north-south transect [*Wofsy et al.*, 2011]. The warm conveyor belt (WCB) provides a mechanism for the atmospheric mixing of strong surface flux signals coming off the east coast of Asia. The WCB is best described by *Pauluis et al.* [2008], who suggest that warm moist air parcels in the midlatitudes of the western Pacific and Atlantic Ocean basins are easily mixed vertically and northward in the midlatitudes because of low vertical stratification and excess latent heat. It should be noted that while WCBs are potentially a key driver for vertical mixing and northward transport of air to PFA, a frequency analysis of WCBs suggests that they are concentrated in the winter months [*Eckhardt et al.*, 2004]. Despite this analysis that suggests WCBs are seasonal, *Parazoo et al.* [2011] used high-resolution models to show that eddy transport from moist midlatitude air masses is an essential component of the large seasonal cycle in CO_2 that is observed throughout the Arctic and thus most likely contributes to the high-altitude seasonal signal that is observed at PFA and to a lesser extent ETL and ESP.

4.2.2. The Large-Scale Implications of the PFA Seasonal Cycle

To appreciate the implications of the large seasonal cycle of CO_2 observed at PFA, it is instructive to look at the amplitude of seasonal cycle in the column mean (0–8000 masl; Figure 22, bottom) and amplitude of seasonal flux (Figure 22, top) from 2013 CarbonTracker (http://www.esrl.noaa.gov/gmd/ccgg/carbontracker/). This picture suggests that the large seasonal amplitude observed at PFA is representative of a large fraction of the high latitudes that do not necessarily correspond with regional surface fluxes. Inspection of annual climatological mass transport integrated from 0 magl to 8000 masl points to the Jet Stream as the low-latitude boundary to this high-latitude feature. It is along this jet that the WCB is most often observed [*Eckhardt et al.*, 2004]. Although PFA is not an arctic site, vertical profiles at this site provide insights into the factors contributing the large and ever increasing amplitude of the

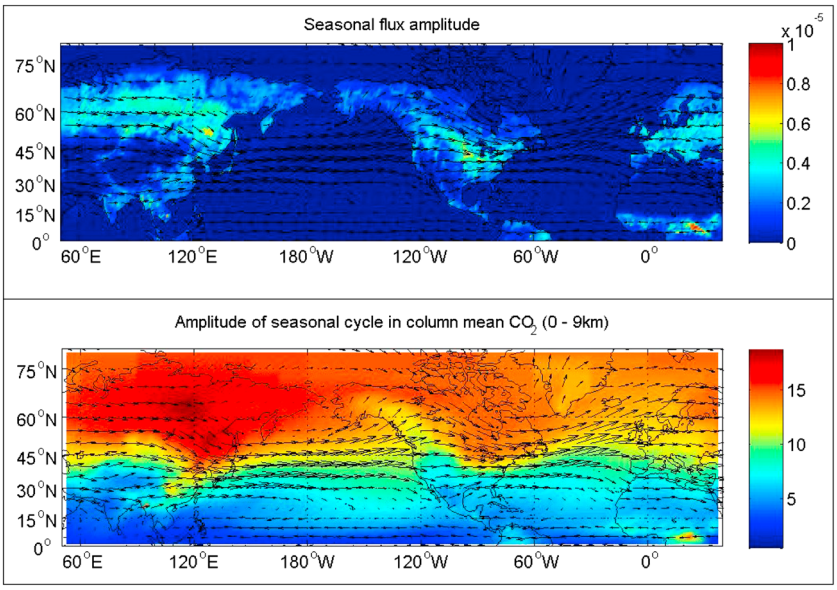

Figure 22. Seasonal amplitude of CO_2 fluxes and column mean CO_2 mole fraction (0 to ~9 km) from CarbonTracker. (top) Seasonal flux amplitude (mol C m^{-2} s^{-1}) overlain with average annual winds. (bottom) Seasonal amplitude of mean column CO_2 (μmol/mol) from (0 to ~9 km) overlain with average climatological winds.

seasonal cycle in the Arctic as pointed out in many studies [e.g., *Graven et al.*, 2013; *Olsen and Randerson*, 2004; *Randerson et al.*, 1997; *Sasakawa et al.*, 2013; *Sawa et al.*, 2012; *Tans et al.*, 1989]. However, the revelation that this signal is likely to originate from lower latitudes adds a further constraint to the idea that meridional transport may be an important ingredient in producing the large seasonal cycle. In contrast, many recent studies have suggested that the boreal region (where PFA is located) is likely to be the largest [e.g., *Graven et al.*, 2013; *Keppel-Aleks et al.*, 2011, 2012; *Olsen and Randerson*, 2004; *Randerson et al.*, 1997] contributor to this the seasonal cycle. These studies suggest that with the extended daylight hours of boreal forests during the summer months, uptake of CO_2 dominates over respiration processes leading to enhanced seasonal cycles of CO_2 in the high latitudes. Both *Randerson et al.* [1997] and *Graven et al.* [2013] suggest that this process is becoming more important as the length of the Boreal growing season increases with warming causing the amplitude of the seasonal cycle at Barrow, AK, and other sites to increase with time.

While many analyses support the fact that the boreal productivity plays a critical role in the large amplitude of the seasonal cycle, the large seasonal cycle, early onset of the drawdown, and well-mixed vertical profiles of CO, CH_4 and N_2O at PFA suggest that lower-latitude influences also have a strong impact on the seasonal cycle of trace gases measured at our northwestern sites. In particular, the low CO and CH_4 mole fractions in the climatology at PFA (Figures 6 and 7) during the summer suggest transport is playing a role in moving depleted air to the higher latitudes from lower latitudes. High values of CO and CH_4 in the winter months also suggest that lower-latitude anthropogenic sources such as those observed at eastern and midcontinent aircraft sites are playing a role in the seasonal cycle since there is little evidence for large local wintertime sources of CO and CH_4 in the Arctic with the prevalence of snow cover and low temperatures [e.g., *Kasischke et al.*, 2002; *Panikov and Dedysh*, 2000].

While the WCB provides a mechanism for both vertically mixing and transporting emissions northward from midlatitudes, modeling studies devoted to understanding transport of carbon monoxide and other pollutants into the Arctic have suggested still other mechanisms that could be contributing to the CO_2 seasonal cycle as well. *Stohl* [2006] suggests that the primary circulation pathway for moving air into the low-temperature dome that makes up the lower troposphere of the Arctic is over northern Eurasia. *Shindell et al.* [2008], on the other hand, suggest, as is argued here, that transport along the east coast of Asia is a more likely path for transport of pollutants such as CO with longer lifetimes (> a few weeks). *Shindell et al.* [2008] argues for this pathway into the Arctic because the high surface fluxes of CO coming from eastern Asian continent are more likely to support the observed high-altitude CO enhancements in

the Arctic. From this perspective, air masses originating from the midlatitudes along the east coast of Asia and North America may have a significant impact on the pollutant concentrations in the Arctic. By inference, these same transport processes that magnify the seasonal cycle of CO and CH_4 in the Arctic may impact the seasonal cycle of CO_2 at higher latitude sites such as PFA.

5. Conclusion

The NOAA/ESRL Global Greenhouse Gas Reference Network Aircraft Program is unique in many respects. In particular, it is the first network consisting of as many as 22 aircraft profiling sites measuring trace gas profiles from altitudes of 300 to 8000 masl for longer than 5 years. A climatology of this data has been produced by using trends in CO_2, CO, CH_4, N_2O, and SF_6 at MLO to map a sparse set of measurements at each site onto a single year. The results of these climatologies show an accumulation of surface fluxes in the lower 4000 masl as air moves from west to east across North America. Temporal deviation in mean wind speeds and direction can have significant effects in the climatological patterns observed at each site. The summertime drawdown in CO_2 is amplified over most of the continent due to lower wind speeds in this season at most sites. At the northerly sites, wintertime northwesterly winds bring air with higher wintertime CO_2 mole fractions into the midlatitudes, which can act to increase the amplitude of the CO_2 seasonal cycle. In opposition, the summer winds from the Gulf Coast transport air with relatively high CO_2 mole fractions into the midlatitudes resulting in a net decrease in the seasonal cycle at the midlatitudes.

Above 4000 m the timing of the seasonal cycle is significantly delayed relative to lower altitudes due to higher wind speeds and slow vertical mixing, which also acts to attenuate the amplitude of the seasonal cycle in the free troposphere. The exception to this separation between the lower 4000 masl and the air above is found at sites in the northwestern part of North America, such as PFA, where the amplitude of the seasonal cycle of CO_2 at high altitudes is significantly enhanced relative to other NOAA/ESRL Global Greenhouse Gas Reference Network Aircraft Program sites that tend to mimic the seasonal cycle of MLO at altitudes over 4000 masl. CO and CH_4 climatologies suggest that transport from lower latitudes plays a significant role in the large seasonal amplitude of CO_2 observed at all altitudes at PFA.

The NOAA/ESRL Global Greenhouse Gas Reference Network Aircraft Program provides a valuable constraint on models, satellite observations, and our understanding of the three-dimensional distributions of long-lived tracers in the atmosphere. For models, this network has not only helped to evaluate vertical mixing but also provided an independent constraint on the mean biospheric uptake of CO_2 over an annual cycle. For satellites, these profiles have become an important benchmark for evaluating spectroscopic estimates of partial and full column trace gas mole fraction averages. It is essential that more effort be made to capture variability of the column at the synoptic timescale in unbiased sampling conditions that do not favor clear days. To this end an expansion of the NOAA/ESRL Global Greenhouse Gas Reference Network Aircraft Program onto commercial aircraft is critical.

Acknowledgments

This work has been funded by the National Oceanic and Atmospheric Administration (NOAA) North American Carbon Program and has benefitted from efforts of the pilots at each site who worked hard to communicate any sampling problems to the NOAA/ESRL Global Greenhouse Gas Reference Network. Flights in the Southern Great Plains were supported by the Office of Biological and Environmental Research of the US Department of Energy under contract DE-AC02-05CH11231 as part of the Atmospheric Radiation Measurement Program (ARM) and Terrestrial Ecosystem Science (TES) Program. This manuscript has also benefitted from the help of Manuel Gloor and two other anonymous reviewers. Data used in this study can be obtained from the corresponding author by email (colm.sweeney@noaa.gov).

References

Andrews, A. E., et al. (2014), CO_2, CO, and CH_4 measurements from tall towers in the NOAA Earth System Research Laboratory's Global Greenhouse Gas Reference Network: Instrumentation, uncertainty analysis, and recommendations for future high-accuracy greenhouse gas monitoring efforts, *Atmos. Meas. Tech.*, *7*(2), 647–687, doi:10.5194/amt-7-647-2014.

Biraud, S. C., M. S. Torn, J. R. Smith, C. Sweeney, W. J. Riley, and P. P. Tans (2013), A multi-year record of airborne CO_2 observations in the US Southern Great Plains, *Atmos. Meas. Tech.*, *6*(3), 751–763, doi:10.5194/amt-6-751-2013.

Bolin, B., and W. Bischof (1970), Variations of carbon dioxide content of atmosphere in Northern Hemisphere, *Tellus*, *22*(4), 431–435.

Bousquet, P., P. Peylin, P. Ciais, C. Le Quere, P. Friedlingstein, and P. P. Tans (2000), Regional changes in carbon dioxide fluxes of land and oceans since 1980, *Science*, *290*(5495), 1342–1346.

Brenninkmeijer, C. A. M., et al. (1999), CARIBIC—Civil aircraft for global measurement of trace gases and aerosols in the tropopause region, *J. Atmos. Oceanic Technol.*, *16*(10), 1373–1383.

Brenninkmeijer, C. A. M., et al. (2007), Civil Aircraft for the regular investigation of the atmosphere based on an instrumented container: The new CARIBIC system, *Atmos. Chem. Phys.*, *7*(18), 4953–4976.

Broecker, W. S., and T. H. Peng (1992), Interhemispheric transport of carbon-dioxide by ocean circulation, *Nature*, *356*(6370), 587–589.

Ciais, P., P. P. Tans, J. W. C. White, M. Trolier, R. J. Francey, J. A. Berry, D. R. Randall, P. J. Sellers, J. G. Collatz, and D. S. Schimel (1995), Partitioning of ocean and land uptake of CO_2 as inferred by delta-C-13 measurements from the NOAA Climate Monitoring and Diagnostics Laboratory Global Air Sampling Network, *J. Geophys. Res.*, *100*(D3), 5051–5070, doi:10.1029/94JD02847.

Conway, T. J., P. P. Tans, L. S. Waterman, and K. W. Thoning (1994), Evidence for interannual variability of the carbon-cycle from the National Oceanic and Atmospheric Administration Climate Monitoring and Diagnostics Laboratory Global Air Sampling Network, *J. Geophys. Res.*, *99*(D11), 22,831–22,855, doi:10.1029/94JD01951.

Coplen, T. B. (1995), New IUPAC guidelines for the reporting of stable hydrogen, carbon, and oxygen isotope-ratio data, *J. Res. Natl. Inst. Stand. Technol.*, *100*(3), 285–285.

Corbin, K. D., A. S. Denning, and N. C. Parazoo (2009), Assessing temporal clear-sky errors in assimilation of satellite CO_2 retrievals using a global transport model, *Atmos. Chem. Phys.*, *9*(9), 3043–3048.

Crevoisier, C., M. Gloor, E. Gloaguen, L. W. Horowitz, J. L. Sarmiento, C. Sweeney, and P. P. Tans (2006), A direct carbon budgeting approach to infer carbon sources and sinks. Design and synthetic application to complement the NACP observation network, *Tellus Ser. B Chem. Phys. Meteorol.*, *58*(5), 366–375, doi:10.1111/j.1600-0889.2006.00214.x.

Crevoisier, C., C. Sweeney, M. Gloor, J. L. Sarmiento, and P. P. Tans (2010), Regional US carbon sinks from three-dimensional atmospheric CO_2 sampling, *Proc. Natl. Acad. Sci. U.S.A.*, *107*(43), 18,348–18,353, doi:10.1073/pnas.0900062107.

Denning, A. S., T. Takahashi, and P. Friedlingstein (1999), Can a strong atmospheric CO_2 rectifier effect be reconciled with a "reasonable" carbon budget?, *Tellus Ser. B Chem. Phys. Meteorol.*, *51*(2), 249–253.

Dlugokencky, E. J., L. P. Steele, P. M. Lang, and K. A. Masarie (1994), The growth-rate and distribution of atmospheric methane, *J. Geophys. Res.*, *99*(D8), 17,021–17,043, doi:10.1029/94JD01245.

Dlugokencky, E. J., K. A. Masarie, P. P. Tans, T. J. Conway, and X. Xiong (1997), Is the amplitude of the methane seasonal cycle changing?, *Atmos. Environ.*, *31*(1), 21–26, doi:10.1016/s1352-2310(96)00174-4.

Draxler, R. R., and G. D. Rolph (2012), HYSPLIT (HYbrid Single-Particle Lagrangian Integrated Trajectory) model access via NOAA ARL READY website, NOAA Air Resources Laboratory, Silver Spring, MD. [Available at http://ready.arl.noaa.gov/HYSPLIT.php.]

Eckhardt, S., A. Stohl, H. Wernli, P. James, C. Forster, and N. Spichtinger (2004), A 15-year climatology of warm conveyor belts, *J. Clim.*, *17*(1), 218–237, doi:10.1175/1520-0442(2004)017<0218:aycowc>2.0.co;2.

Gourdji, S. M., et al. (2012), North American CO_2 exchange: Inter-comparison of modeled estimates with results from a fine-scale atmospheric inversion, *Biogeosciences*, *9*(1), 457–475, doi:10.5194/bg-9-457-2012.

Graven, H. D., et al. (2013), Enhanced seasonal exchange of CO_2 by northern ecosystems since 1960, *Science*, *341*(6150), 1085–1089, doi:10.1126/science.1239207.

Gurney, K. R., et al. (2004), Transcom 3 inversion intercomparison: Model mean results for the estimation of seasonal carbon sources and sinks, *Global Biogeochem. Cycles*, *18*, GB1010, doi:10.1029/2003GB002111.

Heimann, M., and C. D. Keeling (1986), Meridional eddy diffusion-model of the transport of atmospheric carbon-dioxide. 1. Seasonal carbon-cycle over the tropical pacific-ocean, *J. Geophys. Res.*, *91*(D7), 7765–7781, doi:10.1029/JD091iD07p07765.

Inoue, M., et al. (2013), Validation of XCO_2 derived from SWIR spectra of GOSAT TANSO-FTS with aircraft measurement data, *Atmos. Chem. Phys.*, *13*(19), 9771–9788, doi:10.5194/acp-13-9771-2013.

Jacobson, A. R., S. E. M. Fletcher, N. Gruber, J. L. Sarmiento, and M. Gloor (2007), A joint atmosphere-ocean inversion for surface fluxes of carbon dioxide: 1. Methods and global-scale fluxes, *Global Biogeochem. Cycles*, *21*, GB1019, doi:10.1029/2005GB002556.

Kalnay, E., et al. (1996), The NCEP/NCAR 40-year reanalysis project, *Bull. Am. Meteorol. Soc.*, *77*(3), 437–471, doi:10.1175/1520-0477(1996)077<0437:TNYRP>2.0.CO;2.

Karion, A., C. Sweeney, S. Wolter, T. Newberger, H. Chen, A. Andrews, J. Kofler, D. Neff, and P. Tans (2013), Long-term greenhouse gas measurements from aircraft, *Atmos. Meas. Tech.*, *6*(3), 511–526, doi:10.5194/amt-6-511-2013.

Kasischke, E. S., D. Williams, and D. Barry (2002), Analysis of the patterns of large fires in the boreal forest region of Alaska, *Int. J. Wildland Fire*, *11*(2), 131–144, doi:10.1071/wf02023.

Keeling, C. D. (1998), Rewards and penalties of monitoring the Earth, *Annu. Rev. Energy Environ.*, *23*, 25–82.

Keeling, C. D., and M. Heimann (1986), Meridional eddy diffusion-model of the transport of atmospheric carbon-dioxide. 2. Mean annual carbon-cycle, *J. Geophys. Res.*, *91*(D7), 7782–7796, doi:10.1029/JD091iD07p07782.

Keppel-Aleks, G., P. O. Wennberg, and T. Schneider (2011), Sources of variations in total column carbon dioxide, *Atmos. Chem. Phys.*, *11*(8), 3581–3593, doi:10.5194/acp-11-3581-2011.

Keppel-Aleks, G., et al. (2012), The imprint of surface fluxes and transport on variations in total column carbon dioxide, *Biogeosciences*, *9*, 875–891, doi:10.5194/bg-9-875-2012.

Lauvaux, T., et al. (2012), Constraining the CO_2 budget of the corn belt: Exploring uncertainties from the assumptions in a mesoscale inverse system, *Atmos. Chem. Phys.*, *12*(1), 337–354, doi:10.5194/acp-12-337-2012.

Law, B. E., et al. (2002), Environmental controls over carbon dioxide and water vapor exchange of terrestrial vegetation, *Agr. Forest Meteorol.*, *113*(1–4), 97–120, doi:10.1016/s0168-1923(02)00104-1.

Lehman, S. J., et al. (2013), Allocation of terrestrial carbon sources using $^{14}CO_2$: Methods, measurement, and modeling, *Radiocarbon*, *55*(2–3), 1484–1495.

Machida, T., K. Kita, Y. Kondo, D. Blake, S. Kawakami, G. Inoue, and T. Ogawa (2002), Vertical and meridional distributions of the atmospheric CO_2 mixing ratio between northern midlatitudes and southern subtropics, *J. Geophys. Res.*, *108*(D3), 8401, doi:10.1029/2001JD000910.

Machida, T., H. Matsueda, Y. Sawa, Y. Nakagawa, K. Hirotani, N. Kondo, K. Goto, T. Nakazawa, K. Ishikawa, and T. Ogawa (2008), Worldwide measurements of atmospheric CO_2 and other trace gas species using commercial airlines, *J. Atmos. Oceanic Technol.*, *25*(10), 1744–1754, doi:10.1175/2008jtecha1082.1.

Maddy, E. S., C. D. Barnet, M. Goldberg, C. Sweeney, and X. Liu (2008), CO(2) retrievals from the Atmospheric Infrared Sounder: Methodology and validation, *J. Geophys. Res.*, *113*, D11301, doi:10.1029/2007JD009402.

Mikaloff Fletcher, S. E., et al. (2006), Inverse estimates of anthropogenic CO_2 uptake, transport, and storage by the ocean, *Global Biogeochem. Cycles*, *20*, GB2002, doi:10.1029/2005GB002530.

Mikaloff Fletcher, S. E., et al. (2007), Inverse estimates of the oceanic sources and sinks of natural CO_2 and the implied oceanic carbon transport, *Global Biogeochem. Cycles*, *21*, GB1010, doi:10.1029/2006GB002751.

Miller, J. B., S. J. Lehman, S. A. Montzka, C. Sweeney, B. R. Miller, A. Karion, C. Wolak, E. J. Dlugokencky, J. Southon, J. C. Turnbull, and P. P. Tans (2012), Linking emissions of fossil fuel CO_2 and other anthropogenic trace gases using atmospheric (CO_2)-C-14, *J. Geophys. Res.*, *117*, D08302, doi:10.1029/2011JD017048.

Miyamoto, Y., et al. (2013), Atmospheric column-averaged mole fractions of carbon dioxide at 53 aircraft measurement sites, *Atmos. Chem. Phys.*, *13*(10), 5265–5275, doi:10.5194/acp-13-5265-2013.

Montzka, S. A., R. C. Myers, J. H. Butler, J. W. Elkins, and S. O. Cummings (1993), Global tropospheric distribution and calibration scale oF HCFC-22, *Geophys. Res. Lett.*, *20*(8), 703–706, doi:10.1029/93GL00753.

Montzka, S. A., C. M. Spivakovsky, J. H. Butler, J. W. Elkins, L. T. Lock, and D. J. Mondeel (2000), New observational constraints for atmospheric hydroxyl on global and hemispheric scales, *Science*, *288*(5465), 500–503, doi:10.1126/science.288.5465.500.

Montzka, S. A., P. Calvert, B. D. Hall, J. W. Elkins, T. J. Conway, P. P. Tans, and C. Sweeney (2007), On the global distribution, seasonality, and budget of atmospheric carbonyl sulfide (COS) and some similarities to CO_2, *J. Geophys. Res.*, *112*, D09302, doi:10.1029/2006JD007665.

Naik, V., et al. (2013), Preindustrial to present-day changes in tropospheric hydroxyl radical and methane lifetime from the Atmospheric Chemistry and Climate Model Intercomparison Project (ACCMIP), *Atmos. Chem. Phys.*, *13*(10), 5277–5298, doi:10.5194/acp-13-5277-2013.
Nakatsuka, Y., and S. Maksyutov (2009), Optimization of the seasonal cycles of simulated CO(2) flux by fitting simulated atmospheric CO(2) to observed vertical profiles, *Biogeosciences*, *6*(12), 2733–2741.
Nakazawa, T., K. Miyashita, S. Aoki, and M. Tanaka (1991), Temporal and spatial variations of upper tropospheric and lower stratospheric carbon-dioxide, *Tellus Ser. B Chem. Phys. Meteorol.*, *43*(2), 106–117, doi:10.1034/j.1600-0889.1991.t01-1-00005.x.
Nakazawa, T., S. Morimoto, S. Aoki, and M. Tanaka (1993), Time and space variations of the carbon isotopic ratio of tropospheric carbon-dioxide over Japan, *Tellus Ser. B Chem. Phys. Meteorol.*, *45*(3), 258–274, doi:10.1034/j.1600-0889.1993.t01-2-00004.x.
Novelli, P. C., et al. (1998), An internally consistent set of globally distributed atmospheric carbon monoxide mixing ratios developed using results from an intercomparison of measurements, *J. Geophys. Res.*, *103*(D15), 19,285–19,293, doi:10.1029/97JD00031.
Novelli, P. C., A. M. Crotwell, and B. D. Hall (2009), Application of gas chromatography with a pulsed discharge helium ionization detector for measurements of molecular hydrogen in the atmosphere, *Environ. Sci. Technol.*, *43*(7), 2431–2436, doi:10.1021/es803180g.
Olsen, S. C., and J. T. Randerson (2004), Differences between surface and column atmospheric CO_2 and implications for carbon cycle research, *J. Geophys. Res.*, *109*, D02301, doi:10.1029/2003JD003968.
Panikov, N. S., and S. N. Dedysh (2000), Cold season CH_4 and CO_2 emission from boreal peat bogs (West Siberia): Winter fluxes and thaw activation dynamics, *Global Biogeochem. Cycles*, *14*(4), 1071–1080, doi:10.1029/1999GB900097.
Parazoo, N. C., A. S. Denning, J. A. Berry, A. Wolf, D. A. Randall, S. R. Kawa, O. Pauluis, and S. C. Doney (2011), Moist synoptic transport of CO(2) along the mid-latitude storm track, *Geophys. Res. Lett.*, *38*, L09804, doi:10.1029/2011GL047238.
Parrish, D. D., K. C. Aikin, S. J. Oltmans, B. J. Johnson, M. Ives, and C. Sweeny (2010), Impact of transported background ozone inflow on summertime air quality in a California ozone exceedance area, *Atmos. Chem. Phys.*, *10*(20), 10,093–10,109, doi:10.5194/acp-10-10093-2010.
Patra, P. K., et al. (2014), Observational evidence for interhemispheric hydroxyl parity, *Nature*, *513*, 219–223, doi:10.1038/nature13721.
Pauluis, O., A. Czaja, and R. Korty (2008), The global atmospheric circulation on moist isentropes, *Science*, *321*(5892), 1075–1078, doi:10.1126/science.1159649.
Pearman, G. I., and D. J. Beardsmore (1984), Atmospheric carbon-dioxide measurements in the Australian region—10 years of aircraft data, *Tellus Ser. B Chem. Phys. Meteorol.*, *36*(1), 1–24.
Randerson, J. T., M. V. Thompson, T. J. Conway, I. Y. Fung, and C. B. Field (1997), The contribution of terrestrial sources and sinks to trends in the seasonal cycle of atmospheric carbon dioxide, *Global Biogeochem. Cycles*, *11*(4), 535–560, doi:10.1029/97GB02268.
Saeki, T., et al. (2013), Carbon flux estimation for Siberia by inverse modeling constrained by aircraft and tower CO_2 measurements, *J. Geophys. Res. Atmos.*, *118*, 1100–1122, doi:10.1002/jgrd.50127.
Sasakawa, M., T. Machida, N. Tsuda, M. Arshinov, D. Davydov, A. Fofonov, and O. Krasnov (2013), Aircraft and tower measurements of CO_2 concentration in the planetary boundary layer and the lower free troposphere over southern taiga in West Siberia: Long-term records from 2002 to 2011, *J. Geophys. Res. Atmos.*, *118*, 9489–9498, doi:10.1002/jgrd.50755.
Sawa, Y., T. Machida, and H. Matsueda (2012), Aircraft observation of the seasonal variation in the transport of CO_2 in the upper atmosphere, *J. Geophys. Res.*, *117*, D05305, doi:10.1029/2011JD016933.
Shindell, D. T., et al. (2008), A multi-model assessment of pollution transport to the Arctic, *Atmos. Chem. Phys.*, *8*(17), 5353–5372.
Sissenwine, N., M. Dubin, and H. Wexler (1962), The U.S. standard atmosphere, 1962, *J. Geophys. Res.*, *67*(9), 3627–3630, doi:10.1029/JZ067i009p03627.
Stephens, B. B., et al. (2007), Weak northern and strong tropical land carbon uptake from vertical profiles of atmospheric CO_2, *Science*, *316*(5832), 1732–1735, doi:10.1126/science.1137004.
Stohl, A. (2006), Characteristics of atmospheric transport into the Arctic troposphere, *J. Geophys. Res.*, *111*, D11306, doi:10.1029/2005JD006888.
Syakila, A., and C. Kroeze (2011), The global nitrous oxide budget revisited, *Greenhouse Gas Meas. Manag.*, *1*(1), 17–26, doi:10.3763/ghgmm.2010.0007.
Tans, P. P., T. J. Conway, and T. Nakazawa (1989), Latitudinal distribution of the sources and sinks of atmospheric carbon-dioxide derived from surface observations and an atmospheric transport model, *J. Geophys. Res.*, *94*(D4), 5151–5172, doi:10.1029/JD094iD04p05151.
Tans, P. P., I. Y. Fung, and T. Takahashi (1990), Observational constraints on the global atmospheric CO_2 budget, *Science*, *247*(4949), 1431–1438.
Thompson, R. L., et al. (2014), TransCom N2O model inter-comparison—Part 1: Assessing the influence of transport and surface fluxes on tropospheric N2O variability, *Atmos. Chem. Phys.*, *14*(8), 4349–4368, doi:10.5194/acp-14-4349-2014.
Thoning, K. W., P. P. Tans, and W. D. Komhyr (1989), Atmospheric carbon-dioxide at Mauna Loa observatory. 2. Analysis of the NOAA GMCC data, 1974–1985, *J. Geophys. Res.*, *94*(D6), 8549–8565, doi:10.1029/JD094iD06p08549.
Turnbull, J., P. Rayner, J. Miller, T. Naegler, P. Ciais, and A. Cozic (2009), On the use of $^{14}CO_2$ as a tracer for fossil fuel CO_2: Quantifying uncertainties using an atmospheric transport model, *J. Geophys. Res.*, *114*, D22302, doi:10.1029/2009JD012308.
Ueyama, M., H. Iwata, Y. Harazono, E. S. Euskirchen, W. C. Oechel, and D. Zona (2013), Growing season and spatial variations of carbon fluxes of Arctic and boreal ecosystems in Alaska (USA), *Ecol. Appl.*, *23*(8), 1798–1816.
Vaughn, B. H., J. B. Miller, D. F. Ferretti, and J. W. C. White (2004), Stable isotope measurements of atmospheric CO_2 and CH_4, in *Handbook of Stable Isotope Analytical Techniques*, edited by P. de Groot, Elsevier Science.
Wofsy, S. C., H. S. Team, C. M. Team, and S. Team (2011), HIAPER Pole-to-Pole Observations (HIPPO): Fine-grained, global-scale measurements of climatically important atmospheric gases and aerosols, *Philos. Trans. R. Soc. A Math. Phys. Eng. Sci.*, *369*(1943), 2073–2086, doi:10.1098/rsta.2010.0313.
Wunch, D., et al. (2010), Calibration of the total carbon column observing network using aircraft profile data, *Atmos. Meas. Tech.*, *3*(5), 1351–1362, doi:10.5194/amt-3-1351-2010.
Xiong, X., C. Barnet, E. Maddy, C. Sweeney, X. Liu, L. Zhou, and M. Goldberg (2008), Characterization and validation of methane products from the Atmospheric Infrared Sounder (AIRS), *J. Geophys. Res.*, *113*, G00A01, doi:10.1029/2007JG000500.
Xiong, X. Z., C. D. Barnet, Q. L. Zhuang, T. Machida, C. Sweeney, and P. K. Patra (2010), Mid-upper tropospheric methane in the high Northern Hemisphere: Spaceborne observations by AIRS, aircraft measurements, and model simulations, *J. Geophys. Res.*, *115*, D19309, doi:10.1029/2009JD013796.
Yang, Z., R. A. Washenfelder, G. Keppel-Aleks, N. Y. Krakauer, J. T. Randerson, P. P. Tans, C. Sweeney, and P. O. Wennberg (2007), New constraints on Northern Hemisphere growing season net flux, *Geophys. Res. Lett.*, *34*, L12807, doi:10.1029/2007GL029742.
Yurganov, L., W. McMillan, C. Wilson, M. Fischer, S. Biraud, and C. Sweeney (2010), Carbon monoxide mixing ratios over Oklahoma between 2002 and 2009 retrieved from Atmospheric Emitted Radiance Interferometer spectra, *Atmos. Meas. Tech.*, *3*(5), 1319–1331, doi:10.5194/amt-3-1319-2010.